

*Electronic supplementary information (ESI) for:*

**Diffusion-enhanced exciton dissociation in single-material  
organic solar cells**

Nong V. Hoang,<sup>a</sup> Vasileios C. Nikolis,<sup>b,c</sup> Lukasz Baisinger,<sup>b</sup> Koen Vandewal<sup>b,d</sup> and Maxim S.  
Pshenichnikov<sup>a,\*</sup>

<sup>a</sup> *Zernike Institute for Advanced Materials, University of Groningen, Nijenborgh 4, 9747 AG Groningen, the Netherlands*

<sup>b</sup> *Dresden Integrated Center for Applied Physics and Photonic Materials, Technische Universität Dresden, Nöthnitzer Strasse 61, 01187, Dresden, Germany*

<sup>c</sup> *Heliatek GmbH, Treidlerstrasse 3, 01139, Dresden, Germany*

<sup>d</sup> *Institute for Materials Research (IMO-IMOMECA), Hasselt University, Wetenschapspark 1, 3590 Diepenbeek, Belgium*

\* Corresponding author. Email: [m.s.pshenichnikov@rug.nl](mailto:m.s.pshenichnikov@rug.nl) (M.S.P.)

## TABLE OF CONTENTS

- S1. Samples and Experimental methods
- S2. List of samples for PL spectroscopy measurements
- S3. Absorption coefficients of  $\alpha$ -6T films
- S4. Absorption spectrum of CuI
- S5. PL maps of  $\alpha$ -6T films and C<sub>60</sub> film
- S6. PL spectra of  $\alpha$ -6T films
- S7. PL transients at different wavelengths
- S8. PL transients of  $\alpha$ -6T films with and without encapsulation
- S9. PL transients of  $\alpha$ -6T films at different excitation energy densities
- S10. PL transients of  $\alpha$ -6T films on various substrates
- S11. Exciton lifetime in standing and lying  $\alpha$ -6T films
- S12. PL transients of mixed  $\alpha$ -6T films with different thicknesses
- S13. Are excitons trapped at domain boundaries?
- S14. Mean PL energy of neat  $\alpha$ -6T films
- S15. Calculations of energy of dipole-dipole coupling in different molecular stackings
- S16. Details of kinetic Monte-Carlo (KMC) simulations
  - S16.1. General information of KMC simulations
  - S16.2. One-dimensional exciton diffusion
  - S16.3. Diffusion parameters for mixed molecular orientations
  - S16.4. Longitudinal excitation intensity distribution
  - S16.5. Histograms of exciton displacements
  - S16.6. Number of domain boundary crossings
- S17. AFM images of  $\alpha$ -6T films

## S1. Samples and Experimental methods

### S1.1. Sample preparation

The samples fabricated herein, are similar to those used in Reference<sup>1</sup>; the same techniques and approaches were used. In brief, thin films of  $\alpha$ -6T (Lumtec Corp.) were thermally evaporated in a vacuum system with a base pressure of  $10^{-8}$  mbar onto quartz substrates. The evaporation rate was tracked by using quartz crystal microbalances connected with a thickness monitor. The deposition rates were  $0.1 - 0.3 \text{ \AA/s}$  for  $\alpha$ -6T and  $\sim 0.3 \text{ \AA/s}$  for  $C_{60}$ . Based on the studies by Taima *et al.*<sup>2</sup> and Moser *et al.*<sup>3</sup>, we prepared the films of lying and standing molecular orientations as follows. For lying films,  $\alpha$ -6T was deposited on a 2 nm CuI (abcr Gute Chemie) interlayer with a deposition rate of  $0.1 \text{ \AA/s}$  at room temperature. Standing  $\alpha$ -6T films were prepared by growing  $\alpha$ -6T directly on quartz at  $100 \text{ }^\circ\text{C}$  during the deposition. An intermediate case of mixed-orientation  $\alpha$ -6T films was fabricated by the deposition of  $\alpha$ -6T on an unheated quartz substrate ( $\sim 24 \text{ }^\circ\text{C}$ ). The  $\alpha$ -6T films were also deposited on other substrates such as glass or indium tin oxide (ITO); they show similar PL decay times to those on the quartz substrate (see Section S10).

For absorption measurements, several films with the thickness between 10 nm and 70 nm for each  $\alpha$ -6T orientation were prepared. For time-resolved PL measurements,  $\alpha$ -6T films with the thickness of 20, 40 and 70 nm were prepared for each  $\alpha$ -6T orientation (see the sample list in Table S1). In the lying  $\alpha$ -6T film, maintaining the right molecular orientation becomes impossible beyond 40 nm (see Section S11) which limits the sample variety.

To obtain heterojunction films, a 30-nm  $C_{60}$  layer was deposited on top of  $\alpha$ -6T on a half of the substrate area without heating the substrate during the deposition. This ensures that the thickness and molecular orientation of  $\alpha$ -6T are always identical for both neat  $\alpha$ -6T and heterojunction films. The molecular orientation of  $\alpha$ -6T stays constant upon the deposition of  $C_{60}$ , as confirmed by x-ray reflectivity and grazing incidence x-ray diffraction.<sup>4</sup>

After deposition, all samples were encapsulated with an epoxy-glued glass cover in the glovebox under nitrogen environment with very low oxygen and moisture contents ( $<1 \text{ ppm}$ ). Without encapsulation, the samples quickly (in matter of hours) degrade due to environmental factors such as e.g. oxygen and/or moisture (see Section S8).

## S1.2. Thin-film characterization

**Steady-state absorption.** Optical transmission and reflection spectra of  $\alpha$ -6T thin-films with a thickness between 10 nm and 70 nm were recorded with an UV-Vis spectrophotometer (SolidSpec-3700, Shimadzu) using an integrating sphere. From the transmission ( $T$ ) and reflection ( $R$ ) spectra, extinction coefficient ( $\kappa$ ) and refractive index ( $n$ ) were computed using internal software based on a transfer matrix method. The absorption coefficients ( $\alpha$ ) of the  $\alpha$ -6T films were calculated from extinction coefficients using the following equation:<sup>5</sup>

$$\alpha = \frac{4\pi\kappa}{\lambda} \quad (\text{Eq. S1})$$

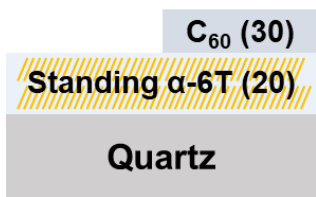
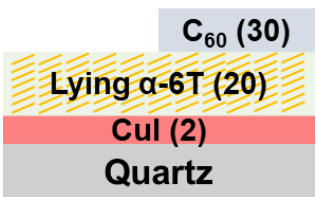
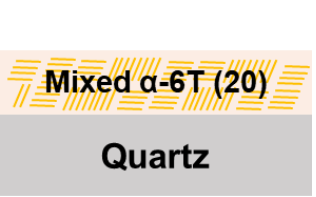
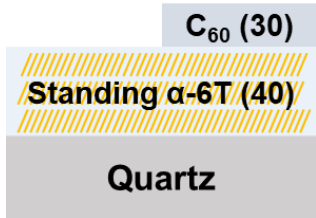
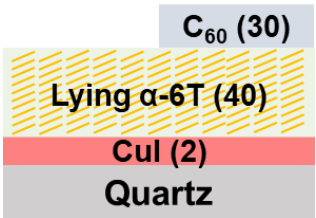
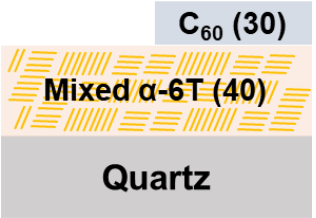
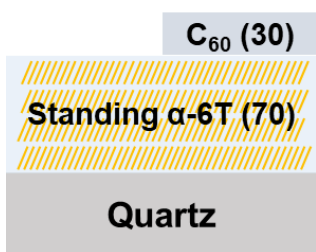
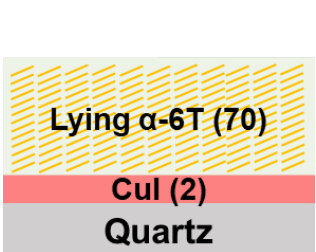
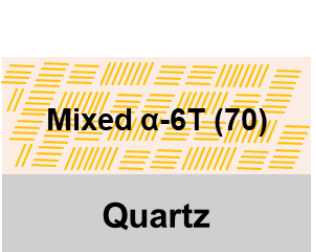
**Time-resolved photoluminescence (PL) measurements.** Time-resolved PL spectroscopy measurements were carried out using a Hamamatsu C5680 streak camera equipped with a Ti:sapphire laser (Mira 900, Coherent). The excitation wavelength at 400 nm was obtained by second harmonic generation of the laser output at 800 nm with 76 MHz repetition rate. The apparatus function of the setup was  $\sim 6$  ps (the standard deviation of a Gaussian apparatus function). In all experiments,  $\alpha$ -6T film samples were measured at room temperature ( $\sim 20$  °C) with normal incidence of the excitation beam to the plane of the film. The excitation laser beam illuminated the substrate side of the samples first and the PL signal was also collected from the same side in the normal incidence geometry. A long-pass dichroic mirror with the cut-off wavelength at 420 nm was used to remove the stray light of the excitation beam to the monochromator entrance slit. PL of samples as a function of the wavelength and delay (PL map) was measured at sufficiently low excitation intensities to avoid exciton-exciton annihilation and/or photodegradation (see Section S9).

**AFM measurements.** AFM images of  $\alpha$ -6T thin-films were obtained using a CombiScope 1000 Scanning Probe Microscope (AIST-NT, Inc.) in a tapping mode. A cantilever with a resonance frequency at  $\sim 250$  kHz and a stiffness of 40 N/m, attached to a Tap300AI-G silicon tip (BudgetSensors), was used. AFM images of  $1 \mu\text{m} \times 1 \mu\text{m}$  and  $5 \mu\text{m} \times 5 \mu\text{m}$  areas were recorded with pixel resolutions of  $512 \times 512$  pixels and  $1024 \times 1024$  pixels, respectively. All measurements were performed at ambient conditions. Afterwards, AFM images were processed using WSxM software.<sup>6</sup>

## S2. List of samples for PL spectroscopy measurements

The list of samples for PL spectroscopy measurements is presented in Table S1.

**Table S1. Summary of the samples of  $\alpha$ -6T films with different thicknesses and molecular orientations.** The thicknesses of the film are shown in parentheses in nm. CuI stands for copper iodine.

Thicknesses	Standing $\alpha$ -6T	Lying $\alpha$ -6T	Mixed $\alpha$ -6T
20 nm	 <p>C<sub>60</sub> (30) Standing <math>\alpha</math>-6T (20) Quartz</p>	 <p>C<sub>60</sub> (30) Lying <math>\alpha</math>-6T (20) CuI (2) Quartz</p>	 <p>Mixed <math>\alpha</math>-6T (20) Quartz</p>
40 nm	 <p>C<sub>60</sub> (30) Standing <math>\alpha</math>-6T (40) Quartz</p>	 <p>C<sub>60</sub> (30) Lying <math>\alpha</math>-6T (40) CuI (2) Quartz</p>	 <p>C<sub>60</sub> (30) Mixed <math>\alpha</math>-6T (40) Quartz</p>
70 nm	 <p>C<sub>60</sub> (30) Standing <math>\alpha</math>-6T (70) Quartz</p>	 <p>C<sub>60</sub> (30) Lying <math>\alpha</math>-6T (70) CuI (2) Quartz</p>	 <p>Mixed <math>\alpha</math>-6T (70) Quartz</p>



**Figure S1. Image of a representative sample.** A 20-nm lying  $\alpha$ -6T layer with a half of the layer covered with C<sub>60</sub>. The size of the sample is  $5 \times 20 \text{ mm}^2$  (inside the encapsulation cap).

### S3. Absorption coefficients of $\alpha$ -6T films

Figure S2 shows absorption coefficient spectra of  $\alpha$ -6T thin-films with standing, lying and mixed molecular orientations. The absorption is the weakest in the standing  $\alpha$ -6T film, the strongest in the lying film; in the mixed-orientation  $\alpha$ -6T film, the absorption coefficient lays in between the two limiting cases. This difference is attributed to the change in direction of the transition dipole moment of the molecules<sup>7,8</sup> with respect to incoming light. The strongest transition dipole moment of  $\alpha$ -6T is directed along the long axis of the molecule,<sup>9,10</sup> and thus it is coupled strongly (weakly) to the electric field polarized parallelly (perpendicularly) to the molecular backbone.<sup>9</sup> Consequently, the film with lying molecules provides much stronger absorption (~10 folds at 400 nm) as compared to the standing film.

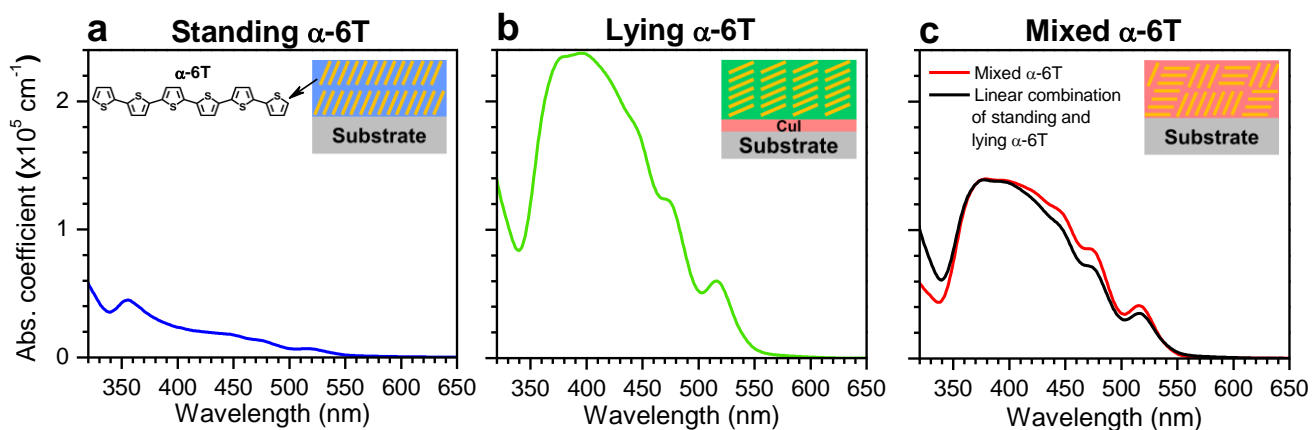


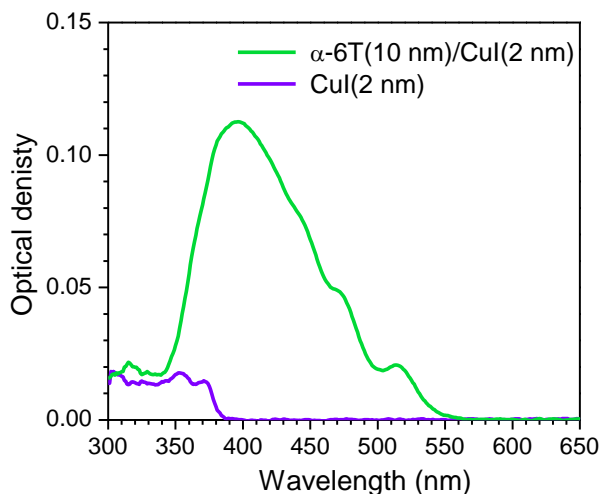
**Figure S2. UV-Vis absorption of  $\alpha$ -6T films with different molecular orientations.** Absorption coefficient spectra of standing (a), lying (b) and mixed (c)  $\alpha$ -6T films. The insets show schematics of sample architectures. The inset in a shows the chemical structure of  $\alpha$ -6T. A linear combination of the spectra of standing and lying  $\alpha$ -6T films with a ratio of 0.47 and 0.53, respectively, is shown in c by the black line. CuI stands for copper iodine with a 2-nm thickness. The absorption of the 2-nm CuI templating interlayer is much weaker as compared to  $\alpha$ -6T absorption (see Figure S3).

The absorption spectra of the three types of the  $\alpha$ -6T films are also different in shape because of different molecular orientations on the films. In the standing film, the absorption spectrum shows a sharp peak at 355 nm. A very similar absorption spectrum was observed in  $\alpha$ -6T single crystals when measured under normal incidence of light onto the (100) face (i.e. an angle of  $65^\circ$  between the molecular backbone and the electric field vector of light).<sup>11,12</sup> When  $\alpha$ -6T molecules in lying

and mixed-orientation films orient in parallel to the substrate, the absorption band between 350 nm and 550 nm is broader because the strongest transition dipole moment is excited.<sup>13–15</sup> The absorption coefficient spectrum of the mixed  $\alpha$ -6T film matches well a linear combination of the spectra of the standing and lying  $\alpha$ -6T films, in a 0.47:0.53 proportion. This indicates that the mixed film consists of domains with standing and lying molecular orientations, not strongly coupled electronically. We note that calculating absorption coefficients from both transmission and reflection spectra (as done here) is required for obtaining the decomposition; doing so from absorption spectra as directly measured by a transmission spectrometer does not yield a satisfactory result.

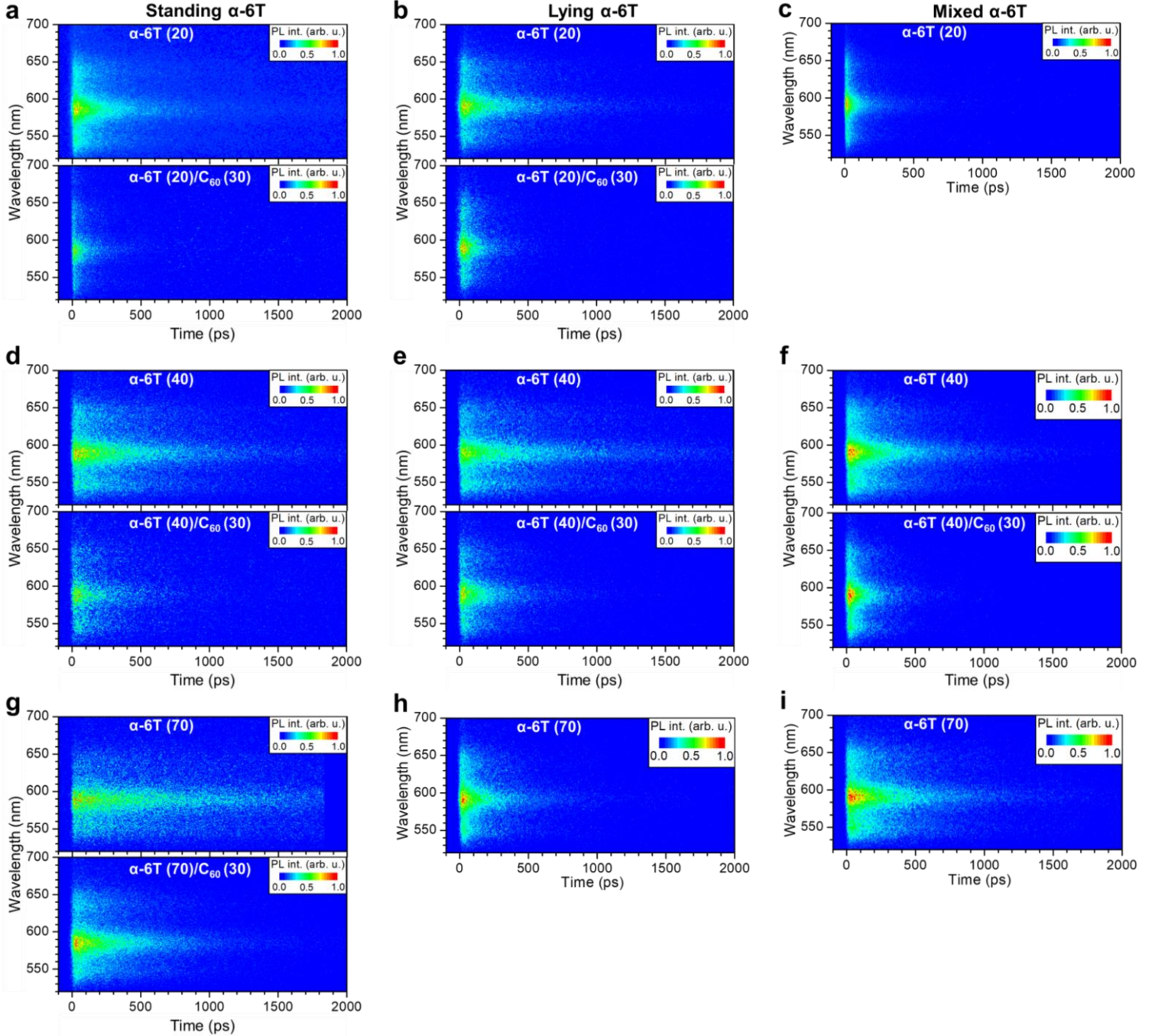
#### S4. Absorption spectrum of CuI

Figure S3 shows absorption spectra of a 2-nm CuI film and a 10-nm lying  $\alpha$ -6T film (the thinnest film). The 2-nm CuI film has a much weaker peak absorption ( $\sim 5$  folds) than the 10-nm lying  $\alpha$ -6T film. Moreover, the CuI film absorbs lights in the wavelength below 385 nm (photon energy of  $\sim 3.2$  eV), indicating that the optical bandgap of CuI is larger than that of  $\alpha$ -6T ( $\sim 2.3$  eV). Therefore, under the excitation at 400 nm (used in this work) CuI in lying  $\alpha$ -6T films is not excited.



**Figure S3. UV-Vis absorption of a CuI thin film.** Absorption spectra of a 2-nm CuI film (purple) and a 10-nm lying  $\alpha$ -6T (green) film (for comparison).

## S5. PL maps of $\alpha$ -6T films and $C_{60}$ film



**Figure S4. Time-resolved PL maps of  $\alpha$ -6T films with different molecular orientations.** PL maps of standing (**a, d, g**), lying (**b, e, h**) and mixed (**c, f, i**)  $\alpha$ -6T films with 20 nm (top panel), 40 nm (middle panel) and 70 nm (bottom panel) thicknesses under 400 nm excitation. The upper and lower graphs show the PL maps of the neat  $\alpha$ -6T and  $\alpha$ -6T/ $C_{60}$  films, respectively. The PL intensity in all maps was normalized to its maximum value.



Figure S4 shows time-resolved PL maps of standing, lying and mixed  $\alpha$ -6T films with different thicknesses and with the presence or absence of the  $C_{60}$  exciton quenching layer. All neat  $\alpha$ -6T films show a similar PL band between 520 nm and 680 nm, which is in a good agreement with previous work.<sup>1</sup> The  $\alpha$ -6T/ $C_{60}$  films show PL spectra similar to those of the neat  $\alpha$ -6T films, indicating that PL of these films does not have contributions from an intermolecular charge transfer state at the  $\alpha$ -6T/ $C_{60}$  interface.

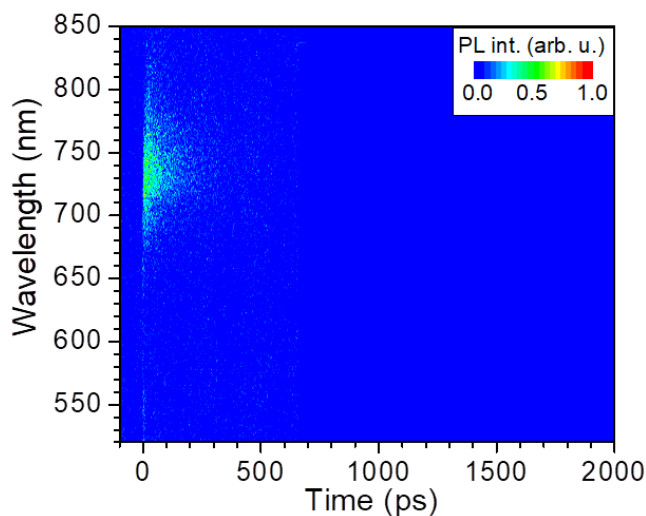


**Figure S5. Time-resolved PL map of a 20-nm  $C_{60}$  film under 400 nm excitation.** The PL intensity was normalized to its maximum value. The integrated signal is more than a factor of 100 weaker than that in Figure S4f.

## S6. PL spectra of $\alpha$ -6T films

Figure S6 shows PL spectra of  $\alpha$ -6T films in two types of the film structures, neat  $\alpha$ -6T and  $\alpha$ -6T/ $C_{60}$  heterojunction, with different  $\alpha$ -6T orientations. All  $\alpha$ -6T films with different molecular orientations and neat/heterojunction structures have similar PL spectra which exhibit three peaks at  $\sim 540$ ,  $\sim 590$  and  $\sim 640$  nm; this is also consistent with Reference <sup>1</sup>. Similarities of time-resolved spectra indicates that there are no structural effects such as molecular orientation or packing on PL.

A PL spectrum of a neat  $C_{60}$  thin film is also shown in Figure S6 for comparison.  $C_{60}$  PL is weak and red-shifted as compared to  $\alpha$ -6T so that it does not interfere with the measurements on  $\alpha$ -6T PL, thereby simplifying the data analysis.

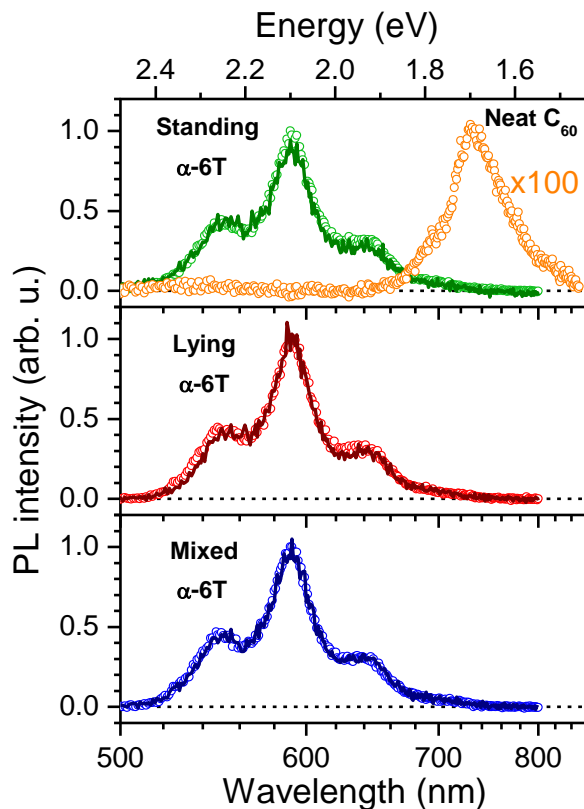


**Figure S6. PL spectra of  $\alpha$ -6T films with different molecular orientations.** PL spectra of neat  $\alpha$ -6T (dotted curves) and  $\alpha$ -6T/ $C_{60}$  heterojunction (solid curves) films with various molecular orientations. The thicknesses of  $\alpha$ -6T and  $C_{60}$  are 40 nm and 30 nm, respectively. The orange dotted curve shows the PL spectrum of a 20-nm neat  $C_{60}$  film multiplied by a factor of 100. The excitation wavelength for all films is 400 nm. The PL spectra were obtained by integrating PL maps (Figures S4 and S5) in the time domain between 0 and 2 ns.

## S7. PL transients at different wavelengths

To confirm that the three PL peaks at ~540, ~590 and ~640 nm originate from the same excited state, PL transients at the wavelengths of these peaks are compared and shown in Figure S7. The PL at these peaks decays with a similar time of ~550 ps and therefore we are attributed to vibronic  $0' \rightarrow 0$ ,  $1' \rightarrow 0$  and  $2' \rightarrow 0$  transitions from the  $S_1$  excited state.<sup>16</sup> Therefore, we conclude that there is no spectral evolution in PL of the  $\alpha$ -6T films.

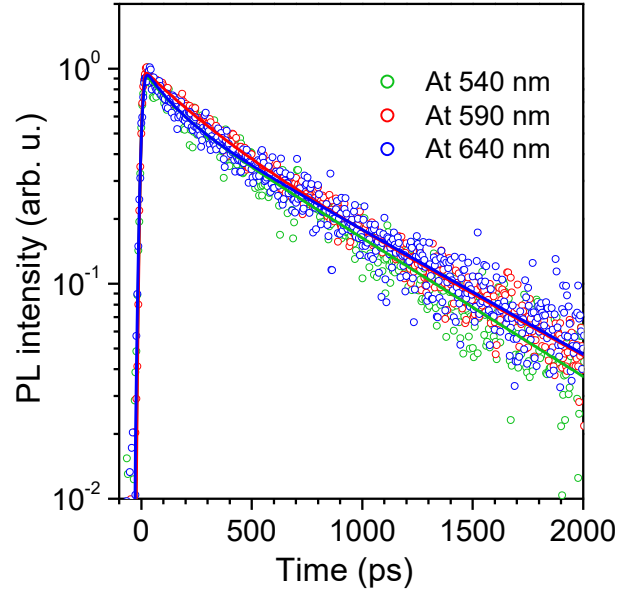


**Figure S7. PL transients at different wavelengths.** Time-resolved PL transients of a 40-nm standing  $\alpha$ -6T film at PL peaks of 540 nm (green), 590 nm (red) and 640 nm (blue). The transients were obtained by integrating the PL maps in the 520-560, 570-610, and 620-660 nm spectral windows, respectively. The solid lines show the fits to a bi-exponential function convoluted with the Gaussian apparatus function. The fitting parameters are summarized in Table S2.

The PL transients of  $\alpha$ -6T films are fitted to a bi-exponential function convoluted to a Gaussian distribution (presenting the apparatus function) (Eq. S2):

$$y = \frac{1}{\sqrt{2\pi\sigma^2}} e^{-\frac{t^2}{2\sigma^2}} \otimes (a_1 e^{-\frac{t}{\tau_1}} + a_2 e^{-\frac{t}{\tau_2}}) \quad (\text{Eq. S2})$$

where  $\sigma$  is the standard deviation of the Gaussian distribution,  $a_1$  ( $a_2$ ) and  $\tau_1$  ( $\tau_2$ ) are the amplitude and decay time of the first (second) exponent, respectively. The sum of all amplitudes is normalized to unity. The average decay time ( $\tau_{ave}$ ) is calculated using Eq. S3:

$$\tau_{ave} = a_1\tau_1 + a_2\tau_2 \quad (\text{Eq. S3})$$

**Table S2. Fitting parameters for PL transients at different wavelengths.** Summary of the decay times and amplitudes of the fits (using Eq. S2) for PL transients of the 40-nm standing  $\alpha$ -6T film at different PL peaks. The sum of all amplitudes is normalized to unity. The average decay time is calculated using Eq. S3:

Parameters	At 540 nm	At 590 nm	At 640 nm
$\sigma$	$10 \pm 1$ ps	$10 \pm 1$ ps	$13 \pm 1$ ps
$a_1$	0.28	0.37	0.35
$\tau_1$	$135 \pm 30$ ps	$250 \pm 30$ ps	$130 \pm 50$ ps
$a_2$	0.72	0.63	0.65
$\tau_2$	$675 \pm 120$ ps	$765 \pm 50$ ps	$750 \pm 50$ ps
$\tau_{ave}$	$520 \pm 100$ ps	$570 \pm 50$ ps	$530 \pm 50$ ps

## S8. PL transients of $\alpha$ -6T films with and without encapsulation

Figure S8 shows PL transients of 40-nm thick  $\alpha$ -6T films of different molecular orientations with and without sample encapsulation; the latter was obtained at the same films outside the encapsulation cap. PL of the films without encapsulation systematically decays faster as compared to their encapsulated counterparts. This is assigned to environmental factors such as oxygen and/or moisture that create exciton traps in the films, thereby shortening PL lifetime. The environmentally-induced traps have even more pronounced effects on exciton quenching than the surface quencher layer of  $C_{60}$ , for instance, the PL decay times for the standing and lying samples become similar for neat and quenched samples,  $\sim 140$  ps. This indicates deep embedding of the traps into the bulk so that the exciton diffusion pathlengths are strongly shortened. The difference is especially striking for the mixed-orientation configuration, where the PL lifetime is reduced from 345 ps in the encapsulating sample to 75 ps in the unencapsulated one. Therefore, encapsulation of  $\alpha$ -6T films is absolutely essential for studying exciton diffusion, quenching and dissociation into charges at heterojunction or domain boundaries.

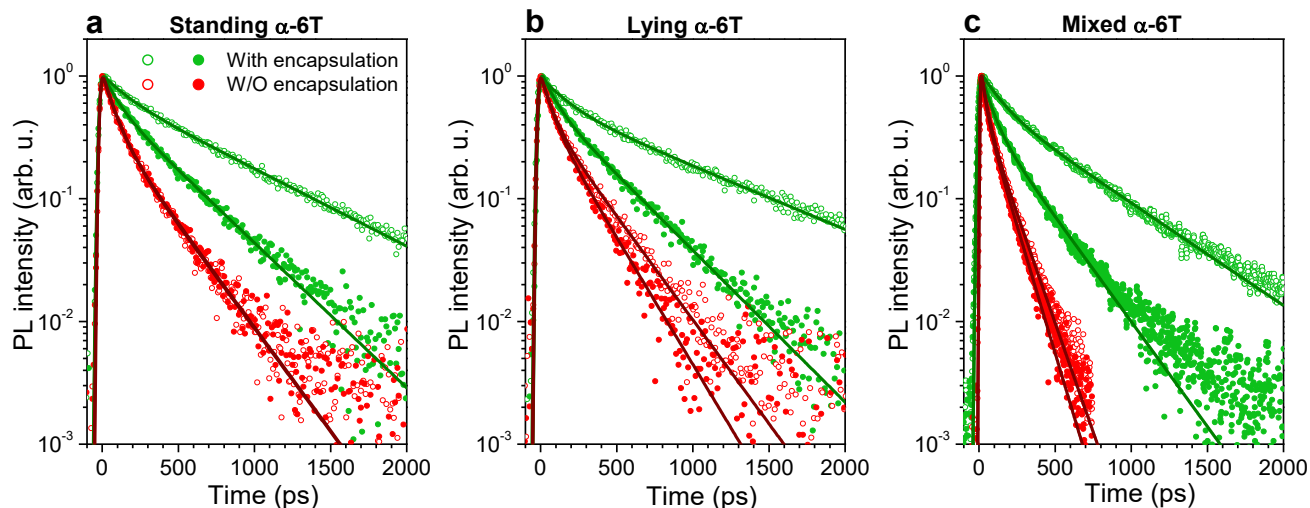


**Figure S8. PL transients of  $\alpha$ -6T films with and without encapsulation.** Time-resolved PL transients of standing (a), lying (b) and mixed (c)  $\alpha$ -6T films with (green) and without (red) encapsulation under 400 nm excitation. The open and filled dot curves show neat  $\alpha$ -6T and  $\alpha$ -6T/ $C_{60}$  heterojunction films, respectively. The thicknesses of  $\alpha$ -6T and  $C_{60}$  in all films is 40 nm and 30 nm, respectively. The transients were obtained by integrating the PL maps in the 520-700 nm spectral window. The solid lines show the best fits to bi-exponential decay functions convoluted to the apparatus function. The average PL decay times are summarized in Table S3.

**Table S3. Fitting parameters for PL transients of  $\alpha$ -6T films with and without encapsulation.**

Summary average decay times (using Eq. S2 and S3) for PL transients of the 40-nm standing, lying and mixed  $\alpha$ -6T films with and without encapsulation.

Samples	Film structure	With encapsulation	Without encapsulation
Standing $\alpha$ -6T	Neat	$530 \pm 10$ ps	$140 \pm 10$ ps
	Heterojunction	$250 \pm 10$ ps	$140 \pm 10$ ps
Lying $\alpha$ -6T	Neat	$560 \pm 10$ ps	$150 \pm 10$ ps
	Heterojunction	$235 \pm 10$ ps	$130 \pm 10$ ps
Mixed $\alpha$ -6T	Neat	$345 \pm 10$ ps	$75 \pm 10$ ps
	Heterojunction	$145 \pm 10$ ps	$65 \pm 10$ ps

## S9. PL transients of $\alpha$ -6T films at different excitation energy densities

As  $\alpha$ -6T films have a large difference in absorption, which depends on the film thickness and molecular orientation, different excitation energy densities are required to observe PL signals. If the excitation energy densities is too high, other processes such as exciton-exciton annihilation,<sup>17</sup> photo-stability and degradation<sup>18,19</sup> can affect the PL signals. In all experiments such excitation energy densities were adjusted to be equivalent of an exciton density of  $\sim 10^{-6} \text{ nm}^{-3}$ , or 1 exciton per  $\sim 55 \text{ nm}$  (at most) in any linear dimension (see Table S5). Therefore, with the  $\sim 50 \text{ nm}$  diffusion length, the exciton-exciton annihilation was safely avoided. No photodegradation was detected either.

To verify the calculations, we performed experiments of the PL intensity dependence on the excitation energy density for all films with different molecular orientations; the representative data for the neat mixed  $\alpha$ -6T film is shown in Figure S9. No changes in PL decay time for the energy density up to  $12 \text{ nJ/cm}^2$  were observed, as the calculations predicted. We note, however, that at higher energy densities we did observe exciton-exciton annihilation (Figure S14).

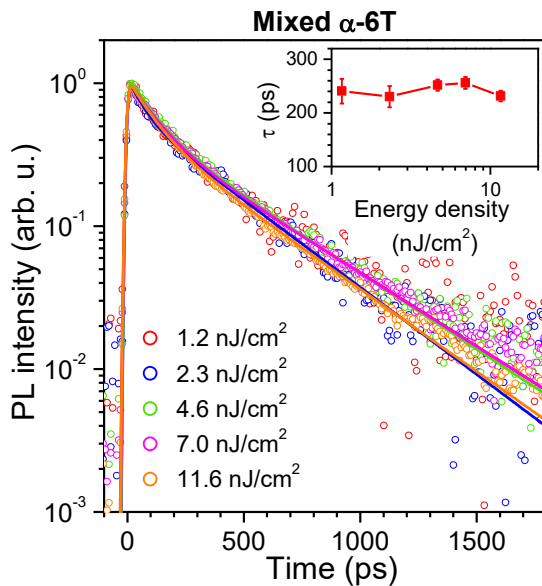


**Figure S9. PL transients of the mixed  $\alpha$ -6T film with various excitation energy densities.** Time-resolved PL transients of a 20-nm thick mixed  $\alpha$ -6T film measured with various excitation energy densities under 400 nm excitation. The transients were obtained by integrating the PL maps in the 520-700 nm spectral window. The solid lines show the fits to a bi-exponential decay function convoluted to the apparatus function. The average PL decay times are summarized in Table S4. The inset shows the average PL decay time as a function of the excitation energy density.

**Table S4. Fitting parameters for PL transients of the mixed  $\alpha$ -6T film at different excitation energy densities.** Summary of the average decay times (using Eq. S2 and S3) for the PL transients of a 20-nm mixed  $\alpha$ -6T film measured with various excitation energy densities under 400 nm excitation.

Energy density	Mixed $\alpha$ -6T
1.2 nJ/cm <sup>2</sup>	240 ± 25 ps
2.3 nJ/cm <sup>2</sup>	230 ± 10 ps
4.6 nJ/cm <sup>2</sup>	252 ± 10 ps
7.0 nJ/cm <sup>2</sup>	256 ± 10 ps
11.6 nJ/cm <sup>2</sup>	230 ± 10 ps

**Table S5. Exciton density in the samples.** Excitation spot diameter is 60  $\mu$ m; excitation wavelength is 400 nm. The first row indicates molecular packing, the second row shows the film thickness.

Parameters	Standing $\alpha$ -6T			Lying $\alpha$ -6T			Mixed $\alpha$ -6T		
	20 nm	40 nm	70 nm	20 nm	40 nm	70 nm	20 nm	40 nm	70 nm
Power [ $\mu$ W]	20	6	40	1	0.4	0.4	20	1.5	0.75
Repetition rate [MHz]	2	2	76	2	2	2	76	2	2
Energy density (nJ/cm <sup>2</sup> )	350	100	20	20	7	7	10	27	13
Absorption	0.05	0.09	0.15	0.38	0.61	0.81	0.24	0.42	0.62
Exciton density [nm <sup>-3</sup> ]	$17 \times 10^{-6}$	$5.0 \times 10^{-6}$	$0.8 \times 10^{-6}$	$6.8 \times 10^{-6}$	$2.2 \times 10^{-6}$	$1.5 \times 10^{-6}$	$2.3 \times 10^{-6}$	$5.8 \times 10^{-6}$	$2.8 \times 10^{-6}$
Average distance between excitons [nm]	55	70	130	85	105	90	150	65	75



## S10. PL transients of $\alpha$ -6T films on various substrates

In this work,  $\alpha$ -6T films were deposited on various substrates for a different set of measurements: atomic force microscopy (on glass and ITO), absorption spectroscopy (on ITO) and time-resolved PL spectroscopy (on quartz). Therefore, it is important to check effects of the  $\alpha$ -6T/substrate interface on exciton diffusion and quenching. Figure S10 shows PL transients of 20-nm thick  $\alpha$ -6T films with different molecular orientations deposited on quartz, ITO and glass substrates.

For each molecular orientation, PL of  $\alpha$ -6T films at various substrates decays quite similarly. The slight difference in decay time is attributed to the change in film surface roughness and/or morphology such as sizes of domains with different molecular orientations, resulting in a different share of domain boundaries to quench excitons. Therefore, the effect of different substrates on exciton diffusion and quenching can be regarded negligibly small.

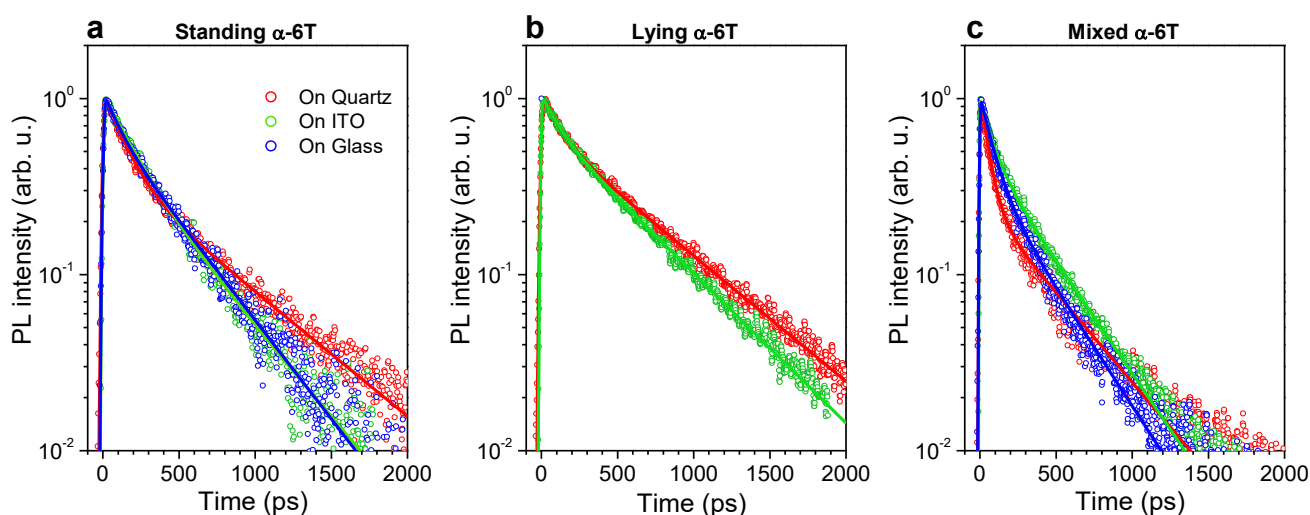


**Figure S10. PL transients of  $\alpha$ -6T films on various substrates.** Time-resolved PL transients of neat standing (a), lying (b) and mixed (c)  $\alpha$ -6T films on quartz (red), ITO (green) and glass (blue) substrates under 400 nm excitation. The film thickness in all films is 20 nm. Note that a 2-nm CuI templating interlayer is used in the lying  $\alpha$ -6T films. The solid lines show the best fits to a bi-exponential decay function convoluted to the apparatus function. The PL decay times are summarized in Table S6.

**Table S6. Fitting parameters for PL transients of  $\alpha$ -6T films on various substrates.**

Summary of decay times and amplitudes of the fits (using Eq. S2) for the PL transients of 20-nm standing, lying and mixed  $\alpha$ -6T films on different substrates. The average decay time is calculated using Eq. S3:

Molecular orientation	Parameters	On Quartz	On ITO	On Glass
Standing $\alpha$ -6T	$\sigma$	$11 \pm 1$ ps	$10 \pm 1$ ps	$10 \pm 1$ ps
	$a_1$	0.63	0.53	0.34
	$\tau_1$	$135 \pm 10$ ps	$190 \pm 20$ ps	$100 \pm 15$ ps
	$a_2$	0.37	0.47	0.66
	$\tau_2$	$615 \pm 15$ ps	$430 \pm 30$ ps	$390 \pm 20$ ps
	$\tau_{ave}$	$310 \pm 15$ ps	$300 \pm 30$ ps	$290 \pm 20$ ps
Lying $\alpha$ -6T	$\sigma$	$11 \pm 1$ ps	$8 \pm 1$ ps	–
	$a_1$	0.40	0.32	–
	$\tau_1$	$110 \pm 10$ ps	$110 \pm 10$ ps	–
	$a_2$	0.60	0.68	–
	$\tau_2$	$610 \pm 10$ ps	$510 \pm 10$ ps	–
	$\tau_{ave}$	$410 \pm 10$ ps	$380 \pm 10$ ps	–
Mixed $\alpha$ -6T	$\sigma$	$5 \pm 1$ ps	$3 \pm 1$ ps	$5 \pm 1$ ps
	$a_1$	0.77	0.49	0.63
	$\tau_1$	$55 \pm 10$ ps	$77 \pm 10$ ps	$80 \pm 10$ ps
	$a_2$	0.23	0.51	0.37
	$\tau_2$	$425 \pm 10$ ps	$340 \pm 15$ ps	$325 \pm 10$ ps
	$\tau_{ave}$	$140 \pm 10$ ps	$210 \pm 15$ ps	$170 \pm 10$ ps

## S11. Exciton lifetime in standing and lying $\alpha$ -6T films

To obtain the intrinsic exciton lifetime in organic films, exciton quenching at the film interfaces should be minimized. This is typically done, for instance, by measuring PL of the thick films at which most excitons decay before reaching the film interfaces.<sup>20</sup> The indication of this is that the PL decay time no longer increases upon increasing the film thicknesses and therefore might be assigned to the exciton lifetime.

Figure S11a shows decay times of PL transients of neat standing and lying  $\alpha$ -6T films with the thickness between 20 and 70 nm. With the increase of the film thickness, the PL decay time becomes longer, up to 0.95 ns for the 70-nm standing film. It seems that an even longer PL time can be obtained with the films thicker than 70 nm. However, to maintain the right molecular orientation the film thickness was limited to 70 nm in the standing films. Apparently, 70 nm is not sufficiently thick to obtain the intrinsic exciton lifetime directly; the only conclusion, we can make, is that the exciton lifetime should be longer than 0.95 ns.

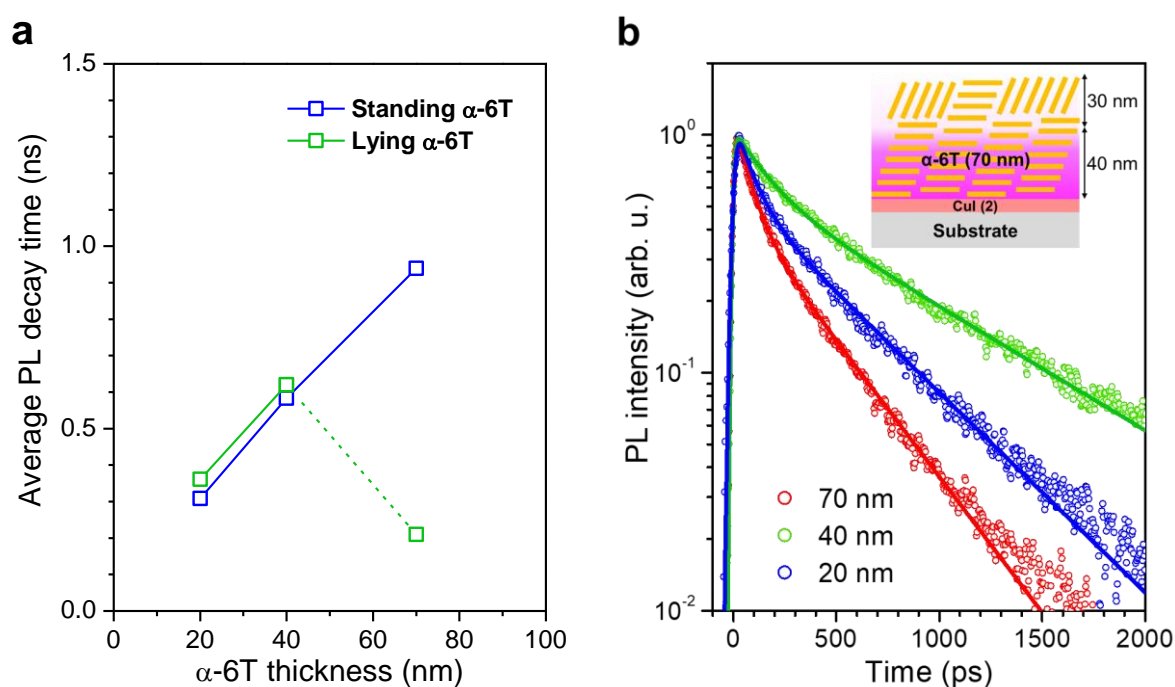


**Figure S11. Exciton lifetime in standing and lying  $\alpha$ -6T films.** **a** Average PL decay times of standing (blue) and lying (green)  $\alpha$ -6T films as a function of the thickness. **b** Time-resolved PL transients of lying  $\alpha$ -6T films with 20 nm (blue), 40 nm (green) and 70 nm (red) thicknesses. The solid lines show the best fits to a bi-exponential decay function convoluted to the apparatus. The PL decay times are summarized in Table S7. The inset shows a sketch of proposed molecular stacking in the 70-nm lying film, indicating the presence of a mixed-orientation film on the top of the underneath lying film.

**Table S7. Fitting parameters for PL transients of lying  $\alpha$ -6T films with different thicknesses.** Summary of decay times and amplitudes of the fits (using Eq. S2) for the PL transients of lying  $\alpha$ -6T films with the 20-nm, 40-nm and 70-nm thicknesses. The average decay time is calculated using Eq. S3:

Parameters	20 nm	40 nm	70 nm
$\sigma$	$15 \pm 1$ ps	$11 \pm 1$ ps	$11 \pm 1$ ps
$a_1$	0.51	0.42	0.58
$\tau_1$	$85 \pm 10$ ps	$160 \pm 10$ ps	$80 \pm 5$ ps
$a_2$	0.49	0.58	0.42
$\tau_2$	$510 \pm 20$ ps	$845 \pm 20$ ps	$390 \pm 20$ ps
$\tau_{ave}$	$290 \pm 20$ ps	$560 \pm 20$ ps	$210 \pm 20$ ps

Figure S11b shows PL transients of lying  $\alpha$ -6T films with 20-nm, 40-nm and 70-nm thicknesses. PL of the 70-nm lying film decays faster than that of the thinner films. This indicates that, besides exciton quenching at film interfaces, excitons are strongly quenched in the bulk of the film, leading to a significant decrease in the PL decay time in 70-nm lying film. As discussed in the main article (Figure 1), PL of mixed-orientation films decays faster than that of lying or standing films with the same thickness. Therefore, the lying architecture should become disrupted by the standing domains thereby forming the mixed phase. Indeed, the effect of the 2-nm CuI templating interlayer at the bottom weakens for thicker films, leading to a formation of the layer with the mixed molecular orientation (the inset in Figure S11b).

Therefore, we conclude that the molecular orientation for the lying film with a thickness higher than 40 nm is no longer preserved. However, for the 20 and 40 nm lying films the exciton lifetime follows that for the standing film. Therefore, we assume that the intrinsic exciton lifetime does not depend on the molecular orientation, and a single value can be used for all orientations. This value, however, still need to be deduced from modelling exciton quenching at the  $\alpha$ -6T/substrate interface.

## S12. PL transients of mixed $\alpha$ -6T films with different thicknesses

Figure S12 shows time-resolved PL transients of the mixed  $\alpha$ -6T films with different thicknesses. Dong *et al.*<sup>1</sup> attributed the decrease in PL decay time to the exciton quenching at boundaries of polycrystalline domains with different molecular orientations. This exciton dissociation results in the faster PL decay in mixed films as compared to that of the films with standing or lying molecular orientation.

Similarity of the transients with 40 nm and 70 nm thicknesses suggests that exciton quenching at the  $\alpha$ -6T/substrate interface is balanced by exciton dissociation at domain boundaries more pronounced in the thicker film. This leads to a more favorable charge yield as shown in Figure 3 of the main article. Somewhat deteriorated quality of the fit at 20 nm thickness is attributed to the surface roughness with the RMS value of  $\sim 8$  nm (Figure S21), which is slightly higher than that of the lying and standing  $\alpha$ -6T films. Therefore, the PL of the mixed  $\alpha$ -6T films displays more distinct bi-exponential decay than that of the lying and standing  $\alpha$ -6T films.

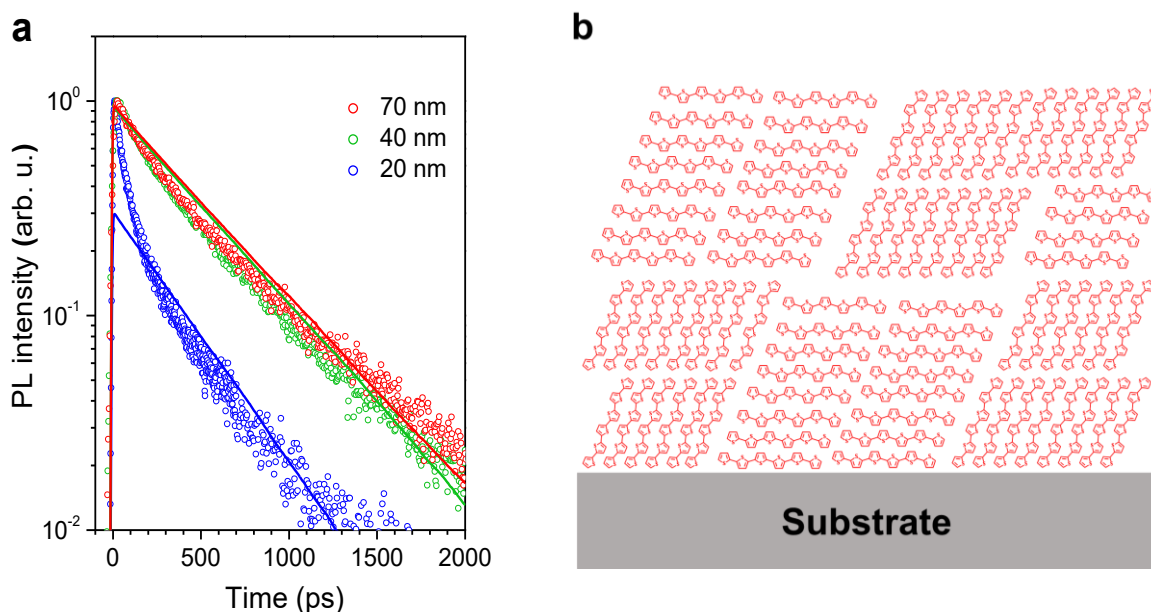


**Figure S12. PL transients of mixed  $\alpha$ -6T films with different thicknesses.** **a** Time-resolved PL transients (dots) of neat mixed  $\alpha$ -6T films with 20-nm (blue), 40-nm (green) and 70-nm (red) thicknesses. The solid lines show the results of KMC simulations, convoluted with the Gaussian apparatus function with standard deviation  $\sigma = 6$  ps. **b** Sketches of molecular stacking in the mixed  $\alpha$ -6T film.

### S13. Are excitons trapped at domain boundaries?

From the KMC simulations (Section S16), we found that exciton quenched at domain boundaries with an extremely small probability of 0.6% (for a 20-nm domain size) but they cross the boundaries many times before dissociating (e.g. inter-domain charge transfer excitons). However, there is another possible scenario that excitons are quenched at domain boundaries with a probability closed to unity, but these quenched states are emissive and thus contribute to PL of the mixed  $\alpha$ -6T films. After some time, the excitons dissociate into charges and therefore stop being emissive. To examine whether this is the case in the mixed  $\alpha$ -6T films, we compared PL transients of the neat  $\alpha$ -6T and the heterojunction film with a 30-nm quenching layer of C<sub>60</sub> at the top.

Figure S13a shows time-resolved PL transients of neat 40-nm thick  $\alpha$ -6T and  $\alpha$ -6T/C<sub>60</sub> heterojunction films, both with mixed  $\alpha$ -6T orientation. If all excitons are quenched at the domain boundaries, PL transients of both films should be similar because the trapped excitons become immobile that therefore cannot reach the C<sub>60</sub> layer. Clearly, this is not the case: the PL transient of the mixed  $\alpha$ -6T/C<sub>60</sub> heterojunction film decays faster than that of the neat  $\alpha$ -6T film (150 ps *vs.* 350 ps). This result indicates that excitons are not quenched at domain boundaries in mixed  $\alpha$ -6T films but keep on travelling through domain interfaces.

To support this conclusion, we run KMC simulations (see Section S16 below) where the excitons were allowed to be quenched (with the probability of unity) at the domain boundaries and produced PL for a time  $\tau_{boundary}$ ; all other parameters such as the exciton lifetime, exciton hopping time, quenching probabilities at film interfaces and domain size were kept intact. First, we determined  $\tau_{boundary} \cong 400$  ps from the best fit to the neat 40-nm thick  $\alpha$ -6T sample (Figure S13a, light green line). Here, the excitons remain within one domain in which they were initially placed (Figure S13b), Secondly, we calculated the PL transient for the heterojunction film (Figure S13a, dark green line). As expected, there is a little difference between the two transients which clearly contradicts the experimental results.

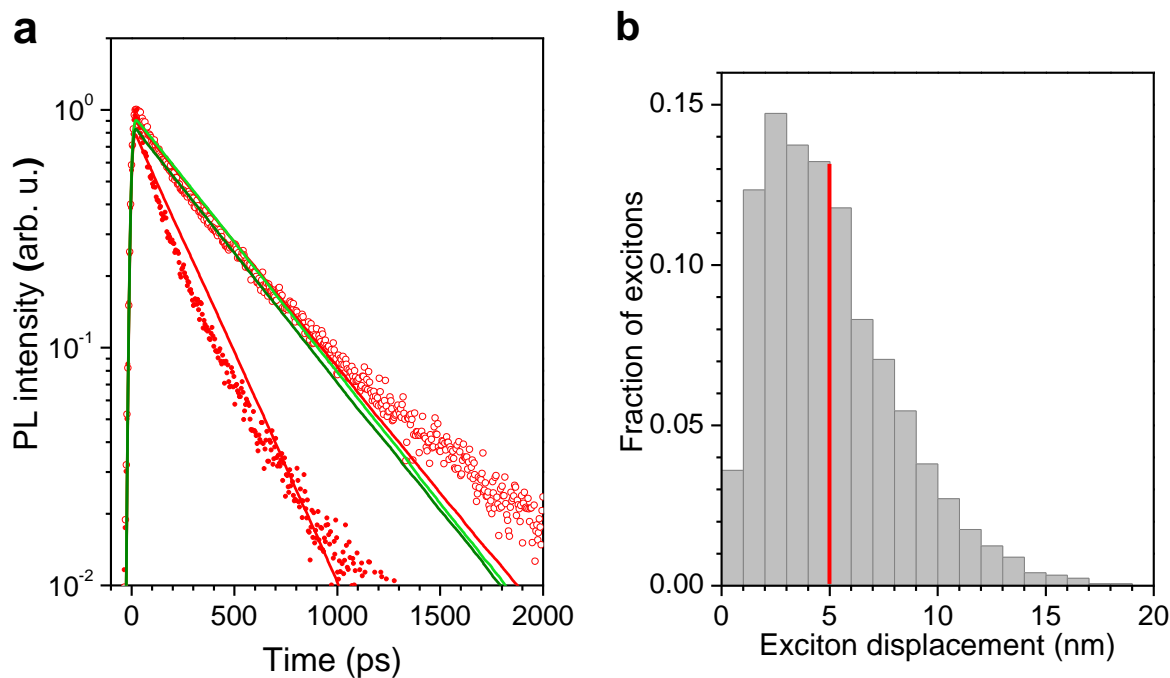


**Figure S13. Exciton mobility in the mixed-orientation films.** **a** Time-resolved PL transients of 40-nm thick mixed  $\alpha$ -6T (open dots) and  $\alpha$ -6T/C60 heterojunction (filled dots) films. The transients were obtained by integrating the PL maps (see Figure S4) in the 520-700 nm spectral range. The red lines show the results of KMC simulations with a low quenching probability of 0.6% at 20-nm domain boundaries. The green lines show the results of KMC simulations of the neat mixed  $\alpha$ -6T (light green) and  $\alpha$ -6T/C60 heterojunction (dark green) films, respectively, in the case of immobile excitons trapped at the domain boundary. All results of KMC simulations are convoluted with the Gaussian apparatus function. **b** Histogram of the exciton displacement in the mixed  $\alpha$ -6T film for the model of immobile excitons immediately trapped at the domain boundary. The red line indicates the mean value of the exciton displacement.

As a complementary to PL transients, the high diffusivity of excitons in the mixed films can be also demonstrated by exciton-exciton annihilation experiments.<sup>21–23</sup> With increasing the exciton density, the distance between two individual excitons shortens. When this distance is comparable to  $L_D$ , excitons are likely to meet and annihilate, resulting in the acceleration of the PL transient. The average inter-exciton distance ( $d$ ) in mixed  $\alpha$ -6T films under laser illumination with different powers can be calculated from Eq. S4 as follows:

$$d = \sqrt{\frac{A \cdot R}{P} \cdot \frac{E_{hv}}{1 - 10^{-OD}}} \quad (\text{Eq. S4})$$

where  $A$  is the area of the illumination spot,  $R$  is the laser repetition rate,  $P$  is the used excitation power,  $E_{hv}$  is the photon energy of the laser source, and  $OD$  is the optical density at the excitation wavelength.

**Table S8. Summary of the parameters for the calculation of the average distance between two excitons.**

Parameters	Values
$A$	$5.28 \cdot 10^9 \text{ nm}^2$
$R$	76 MHz
$E_{hv}$	$4.97 \cdot 10^{-19} \text{ J}$
$P$	8 – 8000 $\mu\text{W}$
$OD$	0.42
$d$	6 – 200 nm

Figure S14 shows a dependence of the average PL decay time of the mixed  $\alpha$ -6T film on the average inter-exciton distance. The average decay time remains constant with the average inter-exciton distance between 70 nm and 200 nm. However, when the average exciton distance is reduced to below 70 nm, the decay time begins to decrease. The average inter-exciton distance of 70 nm is equal to the sum of the diffusion lengths of two closest excitons in mixed  $\alpha$ -6T films ( $\langle L_D \rangle = 35 \text{ nm}$ ). Therefore, this result clearly demonstrates that the excitons retain their diffusivity after passing domain boundaries in mixed films. If excitons had been quenched and immobile at the domain boundaries, the decay time would not have been changed until the threshold of photodegradation.



Finally, we note that the lowest energy density of  $\sim 5 \mu\text{J}/\text{cm}^2$  used in transient absorption spectroscopy in Ref.<sup>1</sup>, clearly falls into the exciton-exciton annihilation regime which might explain the short decay/build-on times of  $\sim 70$  ps obtained therein.

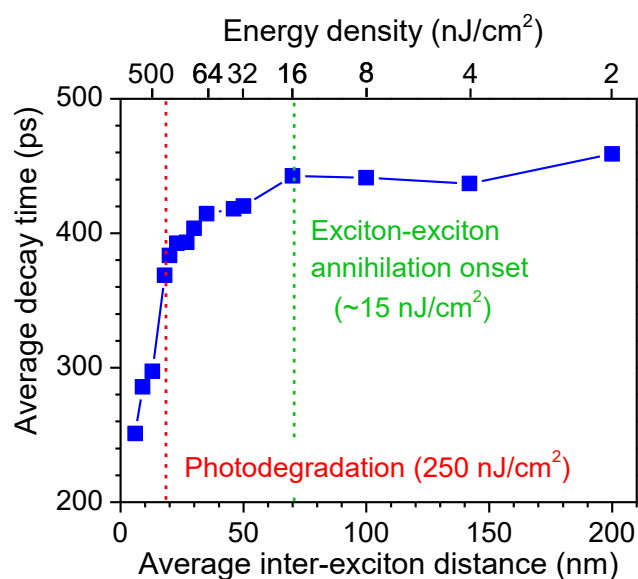


**Figure S14. Exciton-exciton annihilation in the mixed orientation film.** Dependence of the average PL decay time on the average exciton distance. The average PL decay times were obtained from the fits of the PL transients of a 70-nm thick mixed  $\alpha$ -6T film with different excitation energy densities. The average exciton distance ( $d$ ) was calculated from Eq. S4 with parameters summarized in Table S8. The red and green dashed lines depict the onsets for the excitation energy density of photodegradation and exciton-exciton annihilation, respectively. The threshold for photodegradation was assigned to the excitation energy density at which the initial PL decay is no longer recovered after having experienced illumination.

#### S14. Mean PL energy of neat $\alpha$ -6T films

Figure S15 shows the mean PL energies of 40-nm thick  $\alpha$ -6T films with different molecular orientations. PL of all films maintains similar mean PL energy of  $\sim 2.085$  eV with standard deviation of 4 meV in the 0 – 0.5 ns range. This corroborates the value of 6 meV derived from the temperature-dependent PL measurements<sup>16</sup> and also indicates that energetic disorder is negligibly low at room temperature. Therefore, there are no effects of exciton cooling due to relaxation to lower energetic states<sup>24,25</sup> in the samples used.

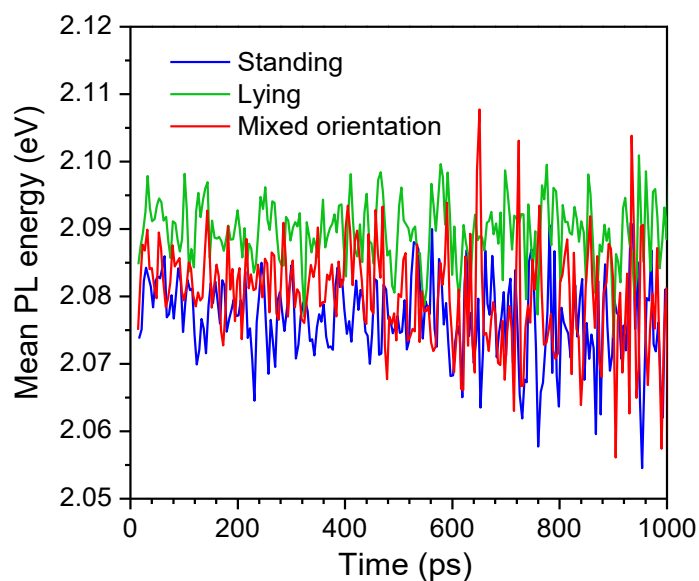


**Figure S15. Mean PL energies of 40-nm neat  $\alpha$ -6T films with various molecular orientations.** The mean energies were calculated as  $\int \omega S(\omega, t) d\omega / \int S(\omega, t) d\omega$  of spectral slices  $S(\omega, t)$  at a particular time  $t$ .

## S15. Calculations of energy of dipole-dipole coupling in different molecular stackings

The transition dipole moment in isolated  $\alpha$ -6T molecules consists of two components with directions along to the molecular axis (L) and orthogonal to molecular axis (M)<sup>26,27</sup> (as sketched in Figure S16a). However, the component along the molecular axis is much stronger than the orthogonal one,<sup>10</sup> and therefore the transition dipole moment of an isolated  $\alpha$ -6T molecule can be simplified as directed along to the molecular axis.

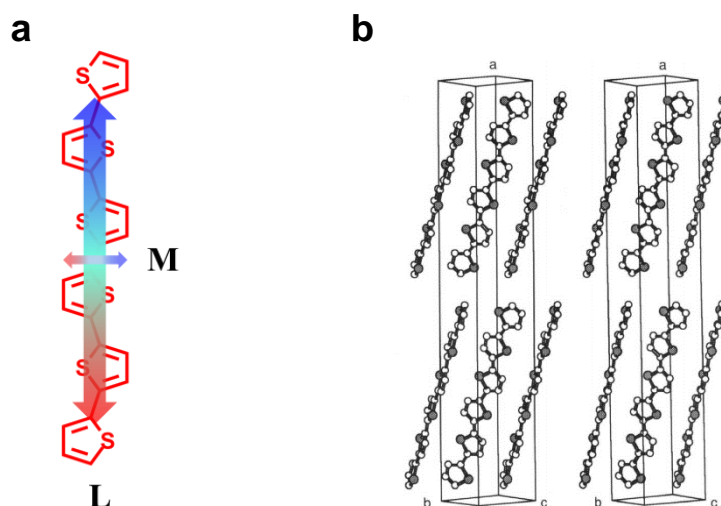


**Figure S16. Transition dipole moments and the crystallographic unit cell of  $\alpha$ -6T.** **a** Representation of the transition dipole moments (colorful arrows) of the isolated  $\alpha$ -6T. **b** Sketch of the  $\alpha$ -6T unit cell. Reproduced from Ref.<sup>27</sup> with permission. Copyright (2021) American Chemical Society.

The dipole-dipole interaction energy  $E$  between two dipoles of a donor (D) and (A) depends (among other parameters) on their distance  $r$  and orientation factor  $K$  between the transition dipole moments of D and A as the following relation:<sup>28</sup>

$$E \sim \frac{K}{r^3} \quad (\text{Eq. S5})$$

The orientation factor  $K$  is calculated as follows:

$$K = (\cos \theta_{DA} - 3 \cos \theta_D \cos \theta_A) \quad (\text{Eq. S6})$$

where  $\theta_{DA}$  is the angle between the transition dipole moments of D and A;  $\theta_D$  and  $\theta_A$  are the angles of the transition dipole moments of D and A with respect to the line joining them, respectively. The transition dipole moments of  $\alpha$ -6T molecules in the unit cell are parallel to one another,<sup>29</sup> resulting in  $\theta_{DA} = 0$ . Therefore, only  $\theta_D$  and  $\theta_A$  affect the calculation of the orientation factor and subsequently the energy coupling.

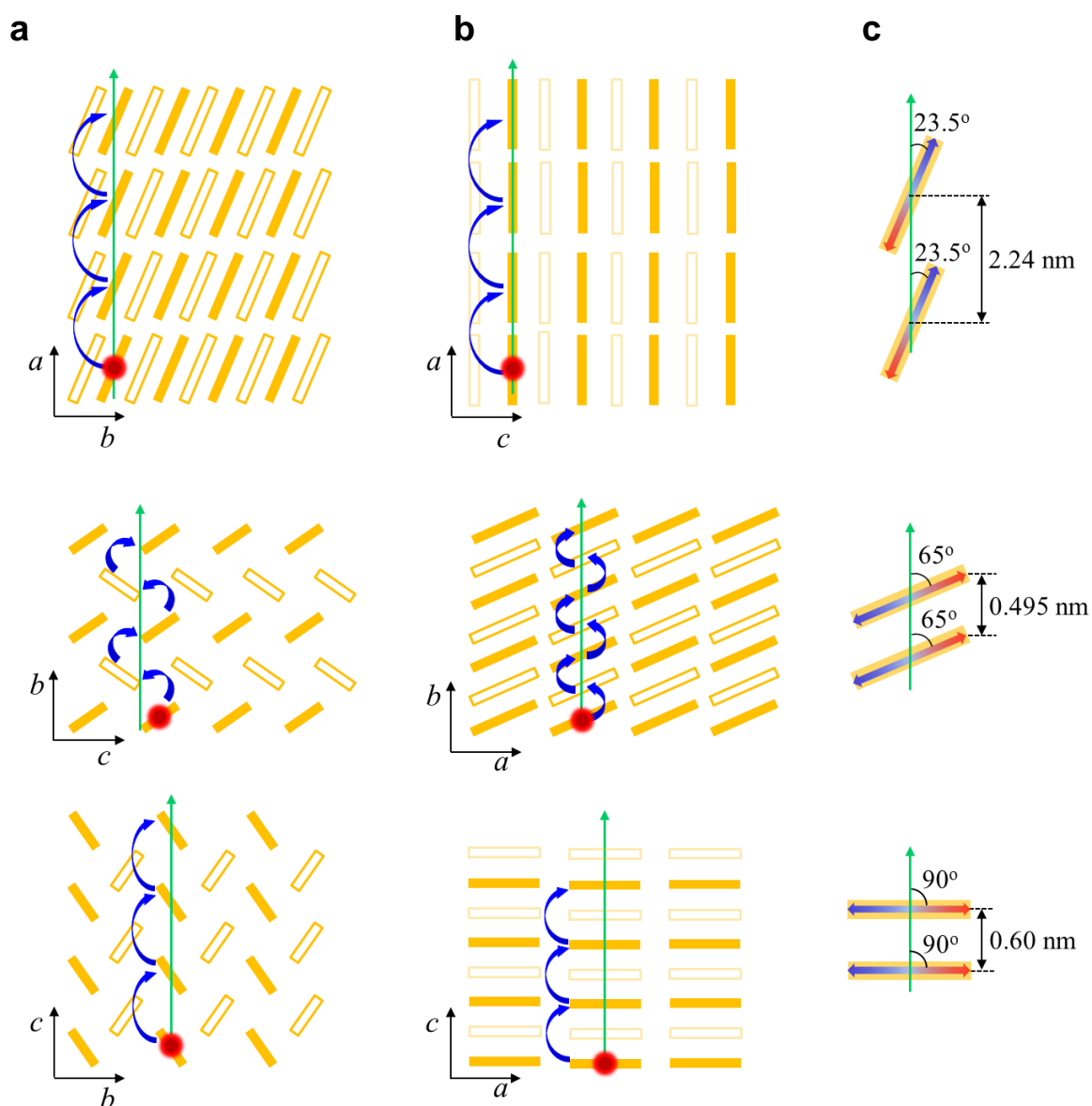


**Figure S17. Schematics of molecular orientations.** (a and b columns) Sketches of molecular stacking in *a*-axis (top panel), *b*-axis (middle panel) and *c*-axis (bottom panel) dimensions from the side view (sketched on the basis of data in Ref.<sup>27</sup>). The open and filled rectangles represent the molecule and its adjacent molecules in lateral dimensions, respectively. The green and blue arrows represent the molecular stacking direction and hopping steps of excitons (red dots), respectively. (c column) Orientations of the two adjacent transition dipole moments (colorful arrows) in *a*-axis (top panel), *b*-axis (middle panel) and *c*-axis (bottom panel) dimensions.

Figure S17 sketches of molecular stacking and orientation of the transition dipole moments in three different axes ( $a$ ,  $b$ ,  $c$ ) of the unit cell. Values of  $\theta_D$  (or  $\theta_A$ ) in  $a$ ,  $b$  and  $c$  dimensions are determined as 23.5, 60 and 90°, respectively.<sup>17</sup> The geometrical factors in energy coupling between two adjacent molecules in  $a$ ,  $b$  and  $c$  axes are summarized in Table S9. The results indicate that the energy coupling between two adjacent molecules in the long-axis molecular stacking ( $a$  axis) is much weaker than that in the herringbone molecular stacking ( $b$  and  $c$  axes). Meanwhile, the energy coupling in the  $b$  axis is similar to that in the  $c$ -axis dimension. Therefore, for KMC simulations, the unknown hopping time (or rate) of excitons between molecules in the  $c$ -axis dimension can be set similar to that in the  $b$ -axis dimension.

**Table S9. Summary of the parameters for different dimensions of the unit cell.**

Parameters	Molecular stacking directions			References
	$a$	$b$	$c$	
Unit cell parameter	44.708 Å	7.851 Å	6.029 Å	<sup>27</sup>
$\theta_{DA}$	0	0	0	-
$\theta_D$	23.5°	65°	90°	-
$\theta_A$	23.5°	65°	90°	-
K	-1.52	0.46	1	-
$r$	2.24 nm	0.495 nm	0.6 nm	<sup>27,30</sup>
Geometrical factor in $ E $	0.14	4.0	4.6	-

## S16. Details of kinetic Monte-Carlo (KMC) simulations

### S16.1. General information of KMC simulations

KMC simulations were based on a stochastic random walk model. The  $\alpha$ -6T film was approximated as a three-dimensional ( $X, Y, Z$ ) grid, consisting of periodic cubic unit cells. For the simulation of the mixed films, the alternated cubic domains of identical sizes of “lying” and “standing” molecular orientations were introduced. As the mean PL energy for neat  $\alpha$ -6T films with various molecular orientations remains constant in time (see Figure S15), energetic disorder<sup>24,25</sup> is weak and therefore is not included in KMC simulations.

When the simulation run started, excitons were created in the grid with a probability proportional to the intensity of the optical electric field in the layer, which was obtained from transfer matrix calculations (see Section S16.4). The excitons might either randomly hop to one of the six closest neighboring sites within a certain hopping time, or decay according to the exciton lifetime  $\tau_0$ . Excitons were reflected back to the grid from the interface facing the air. Excitons are quenched (i). with a probability  $P_{substrate}$  when reaching the  $\alpha$ -6T interface facing the substrate, (ii). with a 100% probability when they reached the top C<sub>60</sub> layer (if any), or (iii). with a probability  $P_{domain}$  when they cross the domain boundary. If the exciton decayed or was quenched, it was removed from the grid. The simulation run continued until the last surviving exciton. By tracking the total number of excitons present in the grid at the given time, a KMC simulated PL transient was calculated.

The KMC simulation was performed first in the standing and lying films with input parameters of  $\tau_0$ ,  $P_{substrate}$ , site-to-site hopping time  $\tau_{hop}$  and the film thickness  $d$ . Simulated transients of samples with different film thicknesses were obtained and used to fit the corresponding experimental PL transients. When all experimental PL transients were fitted,  $\tau_0$ ,  $P_{substrate}$  and  $\tau_{hop}$  in two prime directions were extracted. Then, the KMC simulation was performed in the mixed  $\alpha$ -6T films where  $\tau_0$ ,  $P_{substrate}$  and  $\tau_{hop}$  kept intact. Finally, when all experimental PL transients of the mixed films were fitted with  $P_{domain}$  as the only fitting parameter.

## S16.2. One-dimensional exciton diffusion

To extract exciton diffusion parameters in  $\alpha$ -6T films with standing and lying molecular orientations we used a surface PL quenching method.<sup>31–33</sup> The method requires a set of samples of different film thicknesses with an exciton quenching layer at the film interface.<sup>20,31,34</sup> In this way, the exciton diffusion process probed is a one-dimensional one. Therefore, films with standing and lying orientations will independently provide diffusion coefficients along different directions of molecular packing. We fabricated  $\alpha$ -6T films with various thicknesses on quartz substrates; as an exciton quencher, a C<sub>60</sub> layer was deposited at the top.

Figures S18c,d show time-resolved PL transients of the standing and lying  $\alpha$ -6T films with different thicknesses. The transients from the films of equal thicknesses are quite similar for either molecular packing. Increased bi-exponentiality of the transients as the thickness decreased is attributed to the surface roughness of the films (see Section S17) which becomes more important for the thinner films. For the lying  $\alpha$ -6T films with the thickness above 40 nm, the molecular orientation and packing is no longer preserved, which leads to a drop of the PL decay time (see Section S11).

In general, the PL decay time is not expected to be dependent on film thickness, unless there is exciton quenching at interfaces which results in the decrease of the decay time with the decrease of the thickness. As Figures S18c,d evidence, this is exactly the case so that exciton quenching occurs at the  $\alpha$ -6T/air or  $\alpha$ -6T/substrate interface (or both). As all samples were encapsulated in nitrogen environment, the exciton quenching at the  $\alpha$ -6T/air interface due to oxygen and/or moisture<sup>35</sup> in ambient environment is negligibly low.<sup>31,36,37</sup> Therefore, we assumed that in neat  $\alpha$ -6T films excitons are mainly quenched at the  $\alpha$ -6T/substrate interface.

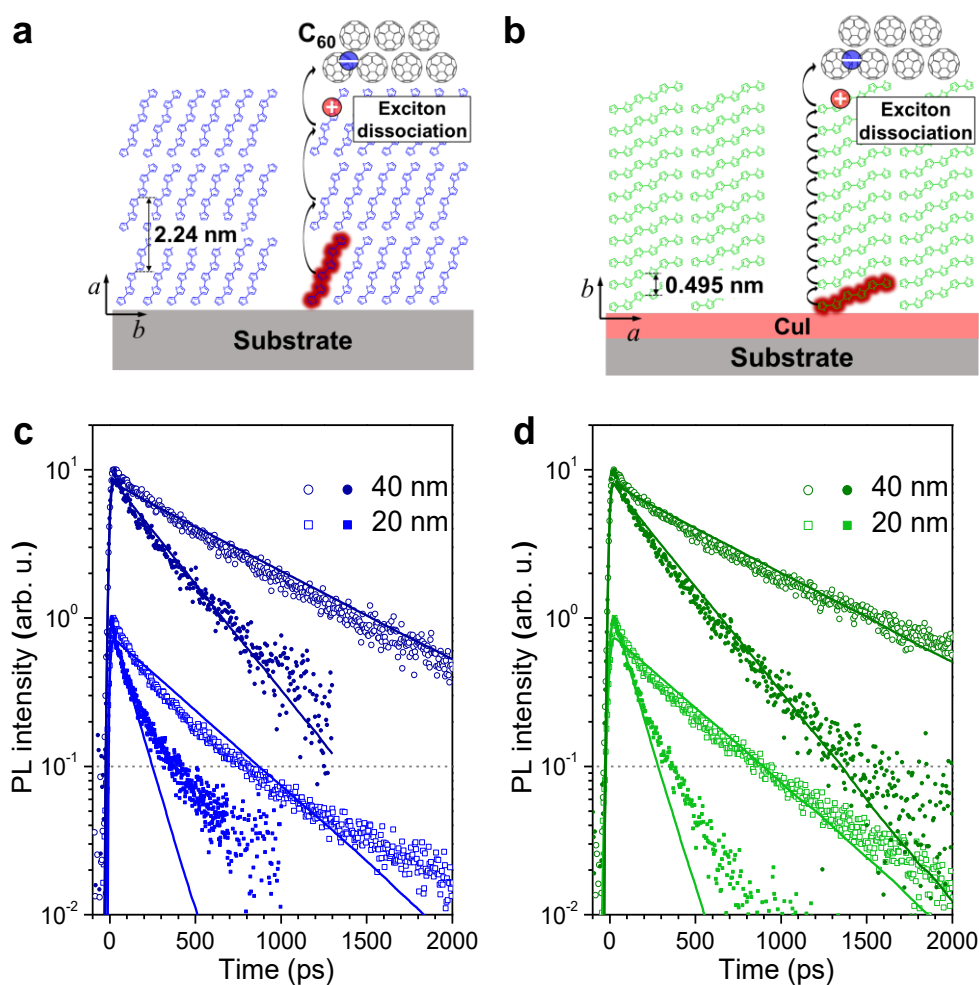


**Figure S18. Exciton diffusion and dissociation in standing and lying  $\alpha$ -6T films.** **a, b** Sketches of molecular stacking of standing (**a**) and lying (**b**)  $\alpha$ -6T films. The curved arrows represent hopping steps of the exciton (red) between two adjacent molecules toward the quenching layer. **c, d** Time-resolved PL transients of the standing (**c**) and lying (**d**)  $\alpha$ -6T films of 20-nm (square dots) and 40-nm (circle dots) thicknesses. The open and filled dots shows the transients of the neat  $\alpha$ -6T and  $\alpha$ -6T/ $C_{60}$  heterojunction films, respectively. The solid lines show the results of KMC simulations, convoluted with the Gaussian apparatus function with standard deviation  $\sigma = 6$  ps. For the sake of clarity, the transients of 40-nm thick  $\alpha$ -6T films are multiplied by 10.

As expected, depositing a  $C_{60}$  quenching layer at the top accelerates the PL transients because the excitons which have diffused to this layer are quenched and therefore lost for PL. Interestingly, the effect of exciton quenching in standing and lying  $\alpha$ -6T films is quite similar despite the fact that in the former case the exciton should pass fewer molecular layers because of the large aspect ratio of the  $\alpha$ -6T molecule. This suggests a balance between the distance along the molecular stacking and the exciton hopping rate which depends on the dipole-dipole



coupling (see Section S15). Similar results have also been previously reported for zinc phthalocyanine<sup>38</sup> and rubrene.<sup>39</sup>

To obtain exciton hopping times (rates) in different dimensions of  $\alpha$ -6T packing, KMC simulations of exciton diffusion and quenching were applied to the standing and lying  $\alpha$ -6T films. The KMC simulations of exciton diffusion in organic semiconductor materials<sup>40-42</sup> require the intrinsic exciton lifetime ( $\tau_0$ ) as an input parameter.<sup>43-45</sup> It is however impossible to accurately measure  $\tau_0$  due to morphological instabilities at large film thicknesses (see Section S17); nevertheless, a lower estimate of  $\tau_0 > 0.95$  ns was obtained directly from the experimental data (see Figure S11a). In the simulations, we use  $\tau_0$  as a fitting parameter, together with the site-to-site hopping time  $\tau_{hop}$  and the quenching probability at the  $\alpha$ -6T/substrate interface  $P_{substrate}$ . The probability of the exciton quenching at the  $\alpha$ -6T/C<sub>60</sub> interface in the heterojunction films was set to unity.

The KMC simulations for PL transients of thicker  $\alpha$ -6T films using the parameters as determined above, yield quite satisfactory results (Figure S18c,d) proving the adequateness of the simple diffusion model applied. The correspondence of KMC simulations and experimental data somehow deteriorates for the thinnest films. This can be explained by effects related to film morphology, including molecular orientation and sizes of crystalline grains, which differ at the very thin film thicknesses. At the lowest thickness (20 nm films),  $\alpha$ -6T films grow as crystalline grains with various sizes with possible defects such as lattice mismatches and voids between the grains.<sup>3,46</sup> These defects might act as exciton quenchers, which reduce the PL decay time and thereby leads to bi-exponential PL transients. With increasing film thickness, the grains expand in lateral dimensions filling up voids and re-arranging molecules to form the well-ordered film. As the KMC model does not take such defects into account, the simulations of the PL transients of thinner  $\alpha$ -6T films do not describe experimental data as good as for the thicker films.

From the best global fits of all PL transients available (Figure S18c,d and Figure 1d,e in the main article), we obtained  $\tau_0 = 1.2 \pm 0.2$  ns and  $P_{substrate} = 5 \pm 2\%$ . The hopping time in the  $a$ -axis dimension was determined as  $\tau_{hop}^a = 1.25 \pm 0.1$  ps, which is a factor of  $\sim 14$  times longer than that in the  $b$ -axis dimension ( $\tau_{hop}^b = 0.09 \pm 0.02$  ps). This result is in good agreement with the coupling energy between two adjacent molecules in the  $a$ - and  $b$ -axis dimensions (see Section S15).

### S16.3. Diffusion parameters for mixed molecular orientations

To obtain the probability of exciton dissociation at a domain boundary, we performed the KMC simulations for the mixed  $\alpha$ -6T films. The grid size in the  $X$  and  $Y$  dimensions was set at 200 points with a periodic boundary condition (i.e. if the exciton leaves one side of the grid, it will appear from the opposite side). The number of the grid point in the  $Z$  dimension was directly proportional to the film thickness, 1 point = 1 nm. The total number of excitons created was smaller than  $10^{-5}$  of the total number of grid points (i.e. 1 exciton in  $\sim 50$  linear grid points) to avoid exciton-exciton annihilation (which was not introduced into the simulations). To account for the molecular aspect ratio, at the end of the simulation run the hopping times were rescaled according to the relation:<sup>47</sup>

$$\tau_{hop} = \frac{1}{2D} \delta^2 \quad (\text{Eq. S7})$$

where  $D$  is the one-dimensional exciton diffusion coefficient and  $\delta$  is the exciton hopping distance (i.e. the distance between the molecules).

The potential problem in simulation of the mixed-orientation films is that the hopping distance between two adjacent molecules in the standing molecular packing direction is much larger ( $\sim 4.5$  folds) than that in the lying molecular packing direction. This leads to an issue of the lattice mismatch at boundaries between domains with different molecular orientations. However, as the diffusion coefficients in the two directions are quite similar (see Section S15), the lattice mismatch issue can be circumvented by considering the same cubic grid divided into the regions assigned to “lying” and “standing” molecular packing. Of course, one should keep in mind that the unit cell does not any longer represent a molecule.

**Table S10. Parameters of KMC simulations for lying, standing and mixed-orientation  $\alpha$ -6T films.**

Parameters		$\alpha$ -6T samples			Sources
		Standing	Lying	Mixed	
Constant input	Film thickness (nm)	20 , 40, 70	20 , 40	20 , 40, 70	Quartz crystal microbalance (sample preparation, Sections S1.1 and S2)
	Hopping distance (nm)	2.24	0.495	1 <sup>(a)</sup>	Crystallographic unit cell (Section S15)
	Domain size (nm)	–	–	20	X-ray diffraction data <sup>1,46,48</sup>
Input for iterative fitting	Exciton lifetime (ns)	1.2 $\pm$ 0.2			Fitting parameter
	Hopping time in the molecular stacking direction (ps per site)	1.25 $\pm$ 0.1	0.09 $\pm$ 0.02	0.3 $\pm$ 0.02	Fitting parameter
	$P_{substrate}$	5 $\pm$ 2%	5 $\pm$ 2%	5 $\pm$ 2%	Fitting parameter
	$P_{domain}$	–	–	0.6 $\pm$ 0.2%	Fitting parameter
Output	Diffusion coefficient $D$ (nm <sup>2</sup> ps <sup>-1</sup> )	2 $\pm$ 0.2	1.4 $\pm$ 0.4	1.6 <sup>(b)</sup>	Eq. S7
	1D diffusion length (nm)	28 $\pm$ 2	23 $\pm$ 2	–	Histogram of 1D exciton displacements (Figure S20)
	3D diffusion length (nm)	48.5	40	35 $\pm$ 5 <sup>(c)</sup>	Histogram of 3D exciton displacements (Figure S21)
	Number of boundary crossings	–	–	60 (130 <sup>(d)</sup> )	Histogram of boundary crossings (Section S16.6)

<sup>(a)</sup> Note that that the unit cell does not any longer represent a molecule (see above text).

<sup>(b)</sup> Mean value of diffusion coefficients into three dimensions.

<sup>(c)</sup> The value is lower than that for the standing and lying molecular orientations because the exciton lifetime is reduced due to exciton dissociation at the domain boundaries.

<sup>(d)</sup> The number in parentheses shows the value obtained from the simulation with the domain size of 10 nm.

#### S16.4. Longitudinal excitation intensity distribution

Figure S19 shows a representative optical field distribution at 400 nm, which is obtained from a transfer matrix calculation, and the distribution of 70,000 initial excitons in a 70-nm standing  $\alpha$ -6T film. The distribution of the initial excitons matches well with the optical distribution in the  $\alpha$ -6T film, indicating that reflection and interference effects are taken into account in the KMC simulations. We calculated similar distribution for each sample and used them in the corresponding KMC simulations. We note however that using a flat intensity profile (as opposed to the one shown in Figure S19), did not result in any substantial changes in the simulated PL transients. A similar observation in regard to the excitation intensity profile was also made previously.<sup>20</sup>

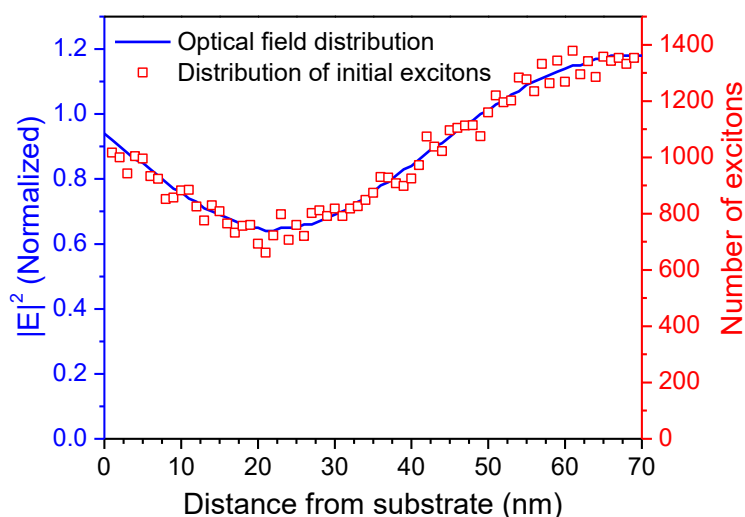
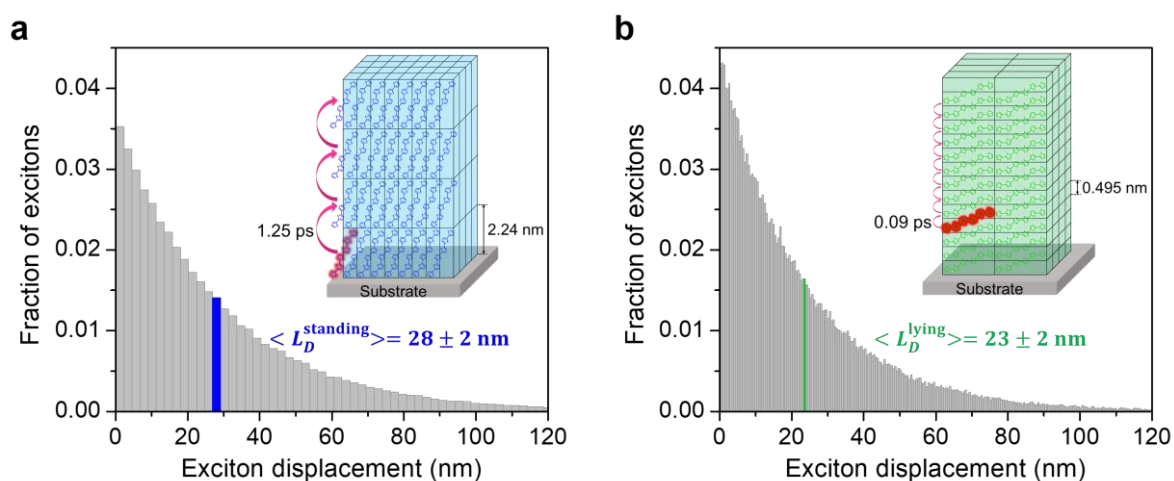


**Figure S19. Longitudinal excitation intensity distribution.** A representative optical field distribution at the 400 nm excitation wavelength (blue curve) and a KMC distribution of 70,000 initial excitons (red dots) in a standing  $\alpha$ -6T film with a 70-nm thickness. The optical field distribution at 400 nm was obtained from the transfer-matrix calculation.

## S16.5. Histograms of exciton displacements

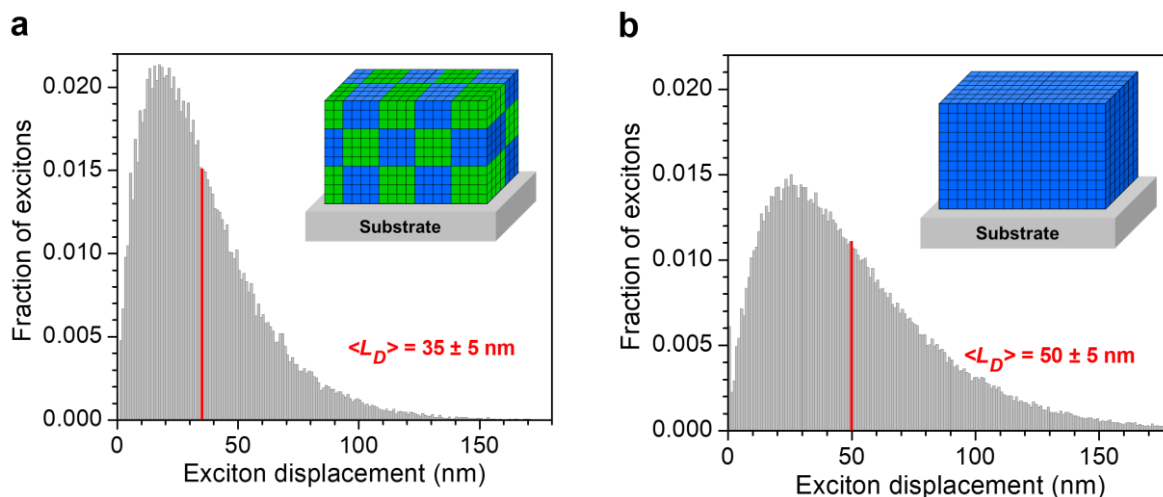
To extract the mean diffusion length  $\langle L_D \rangle$ , the grid size in the  $Z$  dimension was increased until the effect of surface quenching became negligibly small (typically, 400 nm) so that the excitons decayed with their intrinsic lifetime. The coordinates of initial and final positions of an exciton were used to calculate the root-mean-square displacement. With a sufficiently large number of excitons ( $>150,000$  excitons), a histogram of the distribution of the exciton displacement was obtained and the  $\langle L_D \rangle$  is extracted as the mean value of the root-mean-square displacement.

Figure S20 shows histograms of displacements of the exciton decaying with  $\tau_0 = 1.2$  ns in the standing and lying molecular orientations. The one-dimensional (1D) exciton diffusion lengths  $\langle L_D \rangle$  in standing and lying molecular packings are extracted as the mean values of the displacement in  $a$ - and  $b$ -dimensions, respectively.



**Figure S20. One-dimensional exciton diffusion.** Histograms of one-dimensional (along the  $z$ -axis) displacements of the excitons for standing (a) and lying (b) molecular orientations. The 1D exciton diffusion length  $\langle L_D \rangle$  (indicated next to the histograms) is calculated as the mean value of the displacements. The insets show representations of the KMC simulation grids for corresponding films. The bin sizes in the horizontal axis of a and b are set equal to the hopping distances of 2.24 nm and 0.495 nm, respectively.

Figure S21 shows histograms of displacements of the exciton decaying with  $\tau_0 = 1.2$  ns in films with standing and lying orientation. The 3D exciton diffusion length  $\langle L_D \rangle$  is extracted as the mean value of the displacement in 3 dimensions. It was determined as of  $50 \pm 5$  nm for both standing and lying  $\alpha$ -6T films. Due to exciton quenching at the domain boundaries in the mixed film, the  $\langle L_D \rangle$  of  $\alpha$ -6T is shortened to  $35 \pm 5$  nm.



**Figure S21. Three-dimensional exciton diffusion.** Histograms of the exciton displacement in the mixed  $\alpha$ -6T film (a) and in the  $\alpha$ -6T film without quenching at the domain (b). The 3D exciton diffusion length  $\langle L_D \rangle$  is calculated as the mean value of the displacements (as indicated next to the histogram). The insets show schematics of the KMC simulation grid. The domain size is set at 20 nm. The bin sizes in the horizontal axes are set to 1 nm.

## S16.6. Number of domain boundary crossings

To calculate the number of domain boundary crossings, we planted 8000 excitons into the grid and calculated the share of excitons which crossed the boundaries  $N$  times (Figure S22a). The resulting histograms are shown in Figure S22b, for two domain sizes of 10 nm and 20 nm in a 40-nm thick film. The histograms were fitted to an exponential distribution,  $y = e^{-x/\sigma}$ , where  $\sigma$  is the mean number of domain boundary crossings.

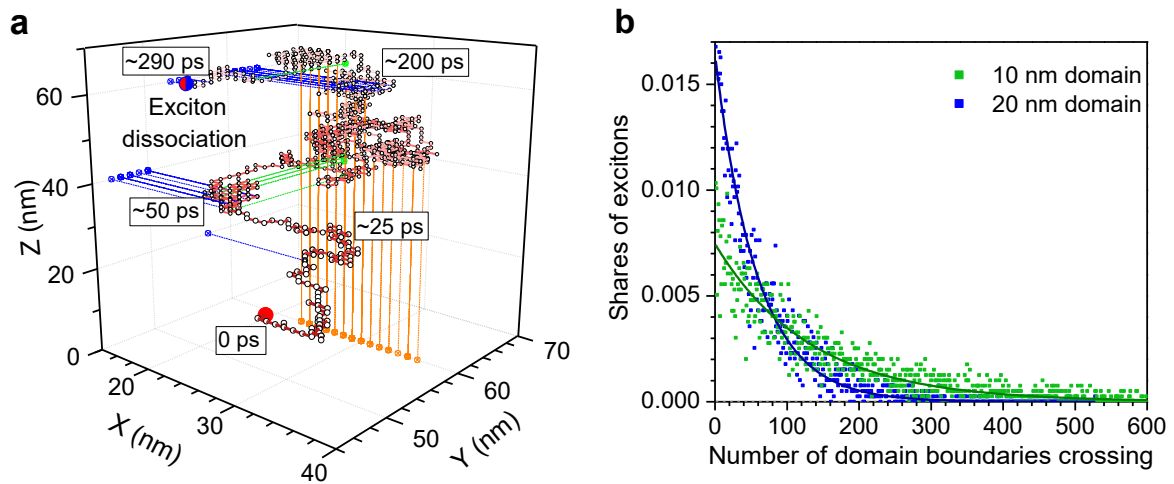


**Figure S22. Domain boundary crossings.** **a** 3D diffusion pathway of a representative exciton in mixed  $\alpha$ -6T films (domain size 20 nm). The green, orange and blue marks indicate the projections of the crossing points of the domain boundaries at XZ, YX and ZY planes, respectively. Times from exciton creation (red dot) are shown along the exciton trajectory in the rectangular boxes. **b** Histogram of the share of domain boundaries where an exciton crosses with the domain sizes of 10 nm (green dots) and 20 nm (blue dots) in a 40-nm thick film. The solid lines show the fits to an exponential function,  $y = e^{-x/\sigma}$  with  $\sigma = 130$  and  $\sigma = 60$  for the histograms for 10 nm and 20 nm domain sizes, respectively.

### S17. AFM images of $\alpha$ -6T films

Figure S23 shows topographic profiles (AFM images) of standing and lying  $\alpha$ -6T films which have quite a similar roughness of 3-6 nm. However, the AFM image exhibits grains with dendritic-like textures in the standing films and ribbon-like textures (~100 nm in width and ~200 nm in length) in the lying film. The difference in texture of the films can be attributed to different molecular orientations while growing  $\alpha$ -6T films. Indeed, it has been reported that needle-like (dendritic-like) structures of  $\alpha$ -6T thin-films on mica mostly contain lying (standing)  $\alpha$ -6T molecules, whereas island-like structures consist of both standing and lying  $\alpha$ -6T molecules.<sup>49,50</sup> The ribbon-like textures in the lying film are quite similar to the needle-like structures of  $\alpha$ -6T films on mica but shorter in length. This is likely due to weaker templating effects of the 2-nm CuI interlayer as compared to mica. Therefore, we can conclude that the surface topography profiles such dendritic-like and ribbon-like textures in standing and lying films, respectively, confirm the desired molecular orientation of  $\alpha$ -6T in the films.

From height histograms and cross-sections of AFM images, an average height and lateral size, respectively, of grains can be estimated. The average grain height for standing and lying films is quite similar at ~5 nm (from the standard deviation of the Gaussian distribution). However, the lateral size of grains in the standing films is estimated between about 200 and 300 nm, which is larger than that in the lying film (~50-100 nm). This can be explained as follows: when growing the standing film, molecules gaining thermal energy (from the heated substrate) become mobile and have more freedom to form densely packed films as compared to those in the lying film, which is deposited at room temperature. This results in a strong lateral growth and in filling underneath layers before growing a new monolayer.



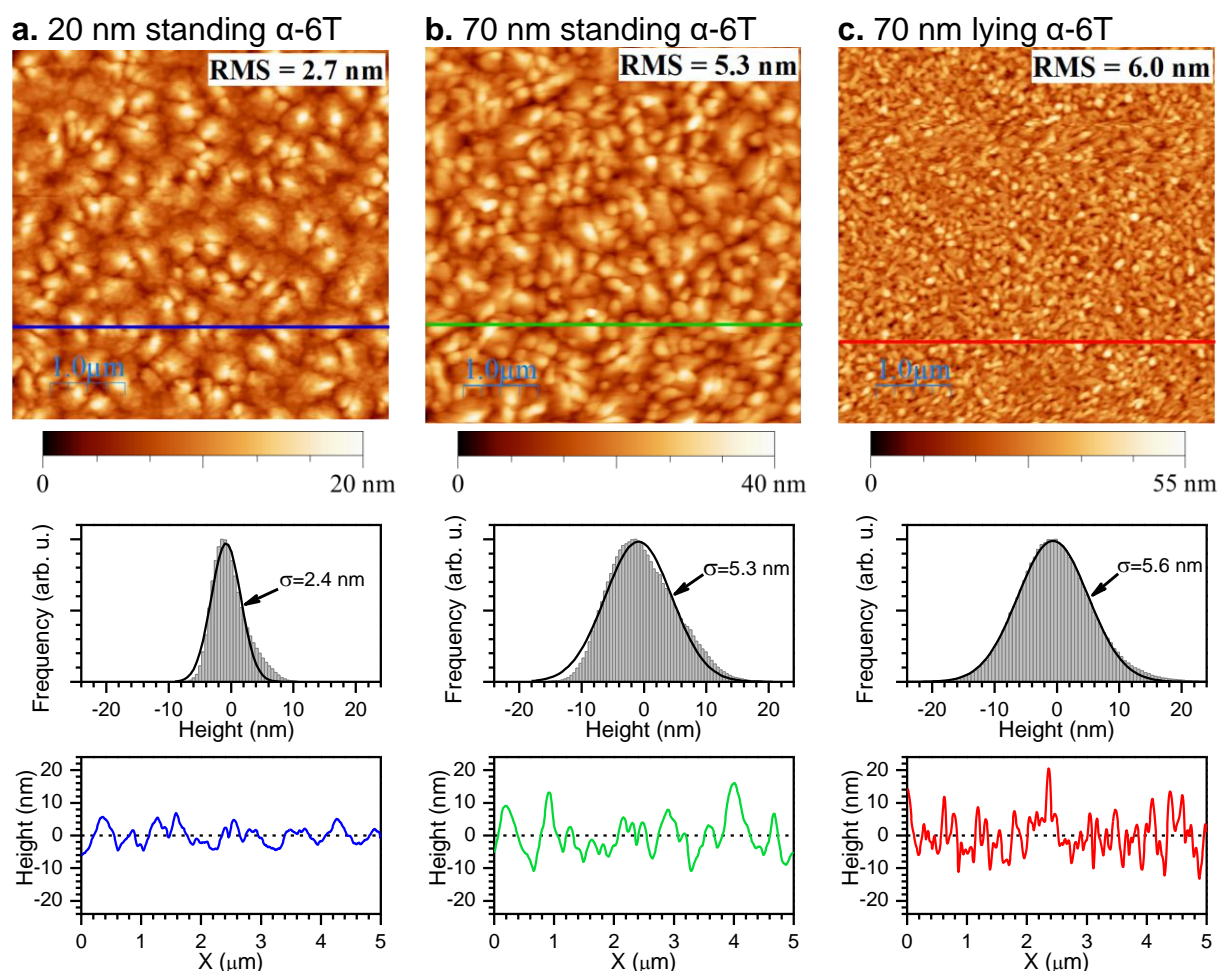


**Figure S23. AFM analysis of the standing and lying  $\alpha$ -6T films.** AFM images (top panel), height histograms (middle panel) and cross-sections (bottom panel) of 20-nm (a) and 70-nm (b) standing and 70-nm lying (c)  $\alpha$ -6T films on ITO substrates. The size of all AFM images is  $5 \mu\text{m} \times 5 \mu\text{m}$ . The root-mean-square (RMS) roughness is shown in the top-right corner of each image. In the histograms, the zero position of the height is set at the average height of the image. The black curves show the fits to the Gaussian function of the height histograms for corresponding films with the standard deviation  $\sigma$ . The cross-sections were taken in lateral directions at the positions indicated as colored solid lines.

Figure S24 shows surface topographic profiles of mixed  $\alpha$ -6T films with 20 nm, 40 nm and 70 nm thicknesses. AFM images exhibit rounded-shape grains with a roughness of  $\sim$ 6-8 nm. This texture is in a good agreement with the  $\alpha$ -6T films on mica at which the film's surface exhibits island-like structures due to coexistence of both standing and lying molecular orientations.<sup>49,50</sup> Hence, the surface topography profiles further confirm the molecular orientation in the mixed  $\alpha$ -6T films. The average grain height slightly increases from the 20 nm film to the 40 nm film and maintains a similar value ( $\sigma \approx 7$  nm) for the 70-nm film. The lateral size of grains in mixed films is similar to that of the lying film ( $\sim$ 50-100 nm).

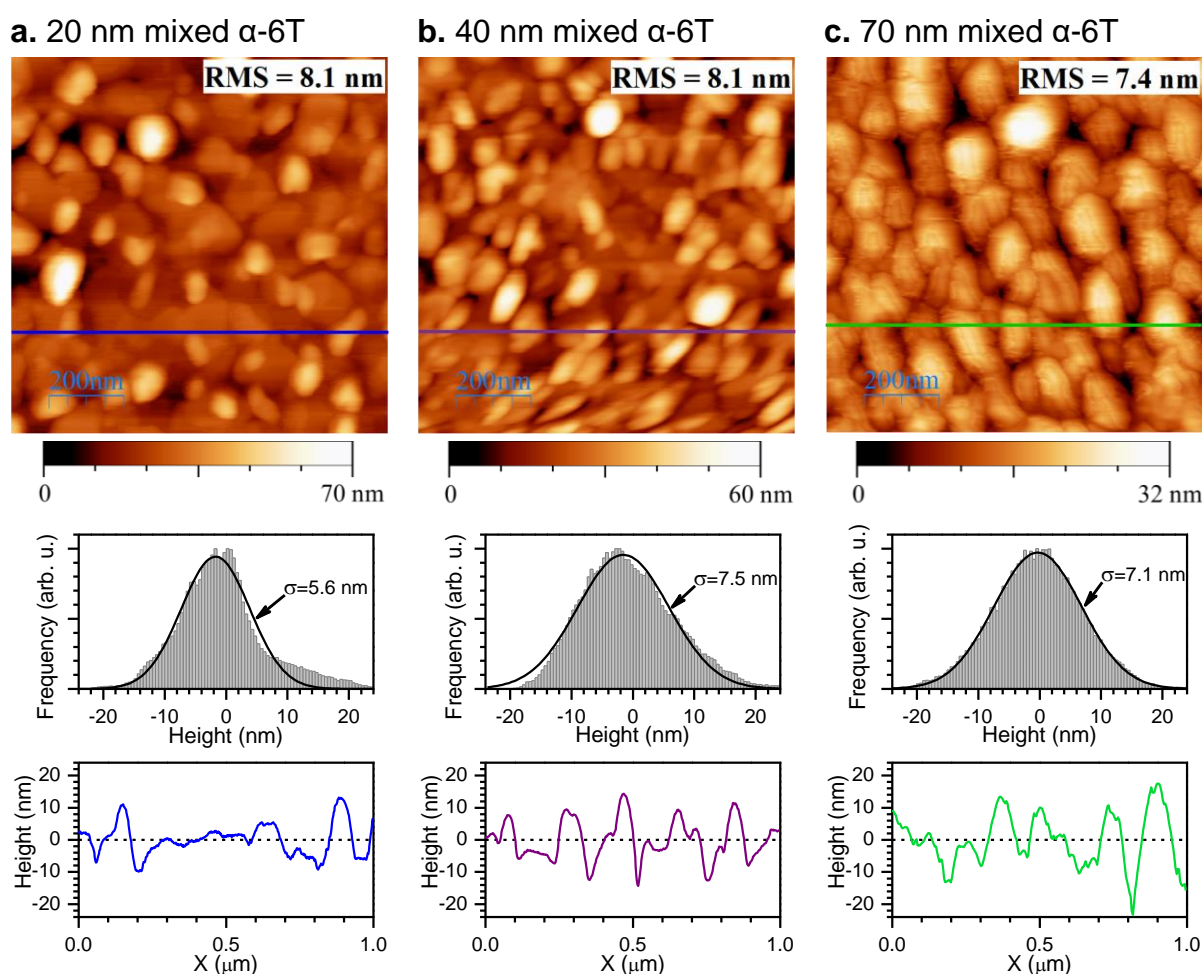


**Figure S24. AFM analysis of the mixed  $\alpha$ -6T films.** AFM images (top panel), height histograms (middle panel) and cross-sections (bottom panel) of mixed  $\alpha$ -6T films with 20 nm (a), 40 nm (b) and 70 nm (c) thicknesses on glass substrates. The size of all AFM images is  $1 \mu\text{m} \times 1 \mu\text{m}$ . The root-mean-square (RMS) roughness is shown in the top-right corner of each image. In the histograms, the zero position of the height is set at the average height of the image. The black curves show the fits to the Gaussian function of the height histograms for corresponding films with the standard deviation  $\sigma$ . The cross-sections were taken in lateral directions at the positions indicated as colored solid lines.

The surface roughness accounts for bi-exponentiality of the PL transient as follows. The early (later) time component causes exciton diffusion toward the  $\alpha$ -6T/air interface with a shorter (longer) distance, for example, towards a valley (peak) of the surface. The ratio of the RMS roughness and the film thickness is  $\sim 2$  times higher for the 20-nm film than for the 70-nm film; and therefore, the rough  $\alpha$ -6T/air interface of the 20-nm film has more impact on exciton quenching than that of the 70-nm film. Therefore, the PL decays become more bi-exponential for the thinner films. The bi-exponential PL decays are even more pronounced for the  $\alpha$ -6T/C<sub>60</sub> heterojunction films. This is due to a higher quenching probability at the  $\alpha$ -6T/C<sub>60</sub> interface than at the  $\alpha$ -6T/air interface, magnifying the exciton quenching at the  $\alpha$ -6T/C<sub>60</sub> interface.

## REFERENCES

- 1 Y. Dong, V. C. Nikolis, F. Talnack, Y. Chin, J. Benduhn, G. Londi, J. Kublitski, X. Zheng, S. C. B. Mannsfeld, D. Spoltore, L. Muccioli, J. Li, X. Blase, D. Beljonne, J. Kim, A. A. Bakulin, G. D. Avino, J. R. Durrant and K. Vandewal, *Nat. Commun.*, 2020, **11**, 4617.
- 2 T. Taima, M. Shahiduzzaman, T. Ishizeki, K. Yamamoto, M. Karakawa, T. Kuwabara and K. Takahashi, *J. Phys. Chem. C*, 2017, **121**, 19699–19704.
- 3 A. Moser, I. Salzmann, M. Oehzelt, A. Neuhold, H. G. Flesch, J. Ivanco, S. Pop, T. Toader, D. R. T. Zahn, D. M. Smilgies and R. Resel, *Chem. Phys. Lett.*, 2013, **574**, 51–55.
- 4 C. Lorch, R. Banerjee, J. Dieterle, A. Hinderhofer, A. Gerlach, J. Drnec and F. Schreiber, *J. Phys. Chem. C*, 2015, **119**, 23211–23220.
- 5 L. A. A. Pettersson, L. S. Roman and O. Inganäs, *J. Appl. Phys.*, 1999, **86**, 487.
- 6 I. Horcas, R. Fernández, J. M. Gómez-Rodríguez, J. Colchero, J. Gómez-Herrero and A. M. Baro, *Rev. Sci. Instrum.*, 2007, **78**, 013705.
- 7 T. Matsushima and H. Murata, *Org. Electron. physics, Mater. Appl.*, 2012, **13**, 222–229.
- 8 T. Matsushima and H. Murata, *J. Appl. Phys.*, 2012, **112**, 024503.
- 9 F. Kouki, P. Spearman, P. Valat, G. Horowitz and F. Garnier, *J. Chem. Phys.*, 2000, **113**, 385–391.
- 10 M. Muccini, E. Lunedei, C. Taliani, D. Beljonne, J. Cornil and J. L. Brédas, *J. Chem. Phys.*, 1998, **109**, 10513–10520.
- 11 S. Möller, G. Weiser and C. Taliani, *Chem. Phys.*, 2003, **295**, 11–20.
- 12 G. Weiser and S. Möller, *Phys. Rev. B*, 2002, **65**, 045203.
- 13 D. Oelkrug, H. J. Egelhaaf and J. Haiber, *Thin Solid Films*, 1996, **284–285**, 267–270.
- 14 M. A. Loi, C. Martin, H. R. Chandrasekhar, M. Chandrasekhar, W. Graupner, F. Garnier, A. Mura and G. Bongiovanni, *Phys. Rev. B*, 2002, **66**, 113101.
- 15 P. Lang, G. Horowitz, P. Valat, F. Garnier, J. C. Wittmann and B. Lotz, *J. Phys. Chem. B*, 1997, **101**, 8204–8211.
- 16 A. Mani, J. Schoonman and A. Goossens, *J. Phys. Chem. B*, 2005, **109**, 4829–4836.

- 17 M. T. Sajjad, A. Ruseckas, L. K. Jagadamma, Y. Zhang and I. D. W. Samuel, *J. Mater. Chem. A*, 2020, **8**, 15687–15694.
- 18 A. Rivaton, A. Tournebize, J. Gaume, P. O. Bussière, J. L. Gardette and S. Therias, *Polym. Int.*, 2014, **63**, 1335–1345.
- 19 T. M. Clarke, C. Lungenschmied, J. Peet, N. Drolet, K. Sunahara, A. Furube and A. J. Mozer, *Adv. Energy Mater.*, 2013, **3**, 1473–1483.
- 20 O. V. Kozlov, F. De Haan, R. A. Kerner, B. P. Rand, D. Cheyins and M. S. Pshenichnikov, *Phys. Rev. Lett.*, 2016, **116**, 057402.
- 21 B. Kriete, J. Lüttig, T. Kunsel, P. Malý, T. L. C. Jansen, J. Knoester, T. Brixner and M. S. Pshenichnikov, *Nat. Commun.*, 2019, **10**, 1–11.
- 22 G. M. Akselrod, Y. R. Tischler, E. R. Young, D. G. Nocera and V. Bulovic, *Phys. Rev. B - Condens. Matter Mater. Phys.*, 2010, **82**, 1–4.
- 23 Y. Firdaus, V. M. Le Corre, S. Karuthedath, W. Liu, A. Markina, W. Huang, S. Chattopadhyay, M. M. Nahid, M. I. Nugraha, Y. Lin, A. Seitkhan, A. Basu, W. Zhang, I. McCulloch, H. Ade, J. Labram, F. Laquai, D. Andrienko, L. J. A. Koster and T. D. Anthopoulos, *Nat. Commun.*, 2020, **11**, 5220.
- 24 A. Serbenta, O. V. Kozlov, G. Portale, P. H. M. Van Loosdrecht and M. S. Pshenichnikov, *Sci. Rep.*, 2016, **6**, 36236.
- 25 G. M. Akselrod, F. Prins, L. V. Poulikakos, E. M. Y. Lee, M. C. Weidman, A. J. Mork, A. P. Willard, V. Bulović and W. A. Tisdale, *Nano Lett.*, 2014, **14**, 3556–3562.
- 26 M. Muccini, E. Lunedei, A. Bree, G. Horowitz, F. Gaenier and C. Taliani, *J. Chem. Phys.*, 1998, **108**, 7327.
- 27 G. Horowitz, B. Bachet, A. Yassar, P. Lang, F. Demanze, J. L. Fave and F. Gamier, *Chem. Mater.*, 1995, **7**, 1337–1341.
- 28 R. E. Dale, J. Eisinger and W. E. Blumberg, *Biophys. J.*, 1979, **26**, 161–194.
- 29 P. Petelenz and M. Andrzejak, *J. Chem. Phys.*, 2000, **113**, 11306.
- 30 G. Nan, Q. Shi, Z. Shuai and Z. Li, *Phys. Chem. Chem. Phys.*, 2011, **13**, 9736–9746.
- 31 D. E. Markov, E. Amsterdam, P. W. M. Blom, A. B. Sieval and J. C. Hummelen, *J. Phys. Chem. A*, 2005, **109**, 5266–5274.
- 32 D. E. Markov, J. C. Hummelen, P. W. M. Blom and A. B. Sieval, *Phys. Rev. B*, 2005,

- 72, 045216.
- 33 O. V. Mikhnenko, F. Cordella, A. B. Sieval, J. C. Hummelen, P. W. M. Blom and M. A. Loi, *J. Phys. Chem. B*, 2009, **113**, 9104–9109.
- 34 P. E. Shaw, A. Ruseckas and I. D. W. Samuel, *Adv. Mater.*, 2008, **20**, 3516–3520.
- 35 L. Lüer, H. J. Egelhaaf, D. Oelkrug, G. Cerullo, G. Lanzani, B. H. Huisman and D. De Leeuw, *Org. Electron.*, 2004, **5**, 83–89.
- 36 Y. Tamai, H. Ohkita, H. Benten and S. Ito, *J. Phys. Chem. Lett.*, 2015, **6**, 3417–3428.
- 37 D. Pelczarski, P. Grygiel and W. Stampor, *Phys. Status Solidi Basic Res.*, 2018, **255**, 1800043.
- 38 B. P. Rand, D. Cheyns, K. Vasseur, N. C. Giebink, S. Mothy, Y. Yi, V. Coropceanu, D. Beljonne, J. Cornil, J. L. Brédas and J. Genoe, *Adv. Funct. Mater.*, 2012, **22**, 2987–2995.
- 39 P. Irkhin and I. Biaggio, *Phys. Rev. Lett.*, 2011, **107**, 1–4.
- 40 I. I. Fishchuk, A. Kadashchuk, S. T. Hoffmann, S. Athanasopoulos, J. Genoe, H. Bässler and A. Köhler, in *AIP Conference Proceedings*, 2014, vol. 1610, pp. 47–52.
- 41 M. E. Kcöse, P. Graf, N. Kopidakis, S. E. Shaheen, K. Kim and G. Rumbles, *ChemPhysChem*, 2009, **10**, 3285–3294.
- 42 J. A. Bjorgaard and M. E. Köse, *J. Phys. Chem. C*, 2014, **118**, 5756–5761.
- 43 S. T. Hoffmann, S. Athanasopoulos, D. Beljonne, H. Bässler and A. Köhler, *J. Phys. Chem. C*, 2012, **116**, 16371–16383.
- 44 H. Van Eersel, P. A. Bobbert and R. Coehoorn, *J. Appl. Phys.*, 2015, **117**, 115502.
- 45 E. M. Y. Lee and W. A. Tisdale, *J. Phys. Chem. C*, 2015, **119**, 9005–9015.
- 46 C. Lorch, R. Banerjee, C. Frank, J. Dieterle, A. Hinderhofer, A. Gerlach and F. Schreiber, *J. Phys. Chem. C*, 2015, **119**, 819–825.
- 47 S. Chandrasekhar, *Rev. Mod. Phys.*, 1943, **15**, 1–89.
- 48 U. Hörmann, C. Lorch, A. Hinderhofer, A. Gerlach, M. Gruber, J. Kraus, B. Sykora, S. Grob, T. Linderl, A. Wilke, A. Opitz, R. Hansson, A. S. Anselmo, Y. Ozawa, Y. Nakayama, H. Ishii, N. Koch, E. Moons, F. Schreiber and W. Brütting, *J. Phys. Chem. C*, 2014, **118**, 26462–26470.

- 49 M. Radziwon, M. Madsen, F. Balzer, R. Resel and H. G. Rubahn, *Thin Solid Films*, 2014, **558**, 165–169.
- 50 C. Simbrunner, G. Hernandez-Sosa, M. Oehzelt, T. Djuric, I. Salzmann, M. Brinkmann, G. Schwabegger, I. Watzinger, H. Sitter and R. Resel, *Phys. Rev. B*, 2011, **83**, 115443.